Thermally-induced Deformation of Multi-layered Materials: Analytical and Engineering Formulations

by

Ching-Te Lin

Submitted to the Department of Materials Science and Engineering
in partial fulfillment of the requirements for the degree of

Master of Science in Materials Science and Engineering

at the

MASSACHUSETTS INSTITUTE OF TECHNOLOGY

Feburary 1996

Author .....
Department of Materials Science and Engineering
January 12, 1996

Certified by .....
Subra Suresh
Professor
Thesis Supervisor

Accepted by .....
Michael F. Rubner
Chairman, Departmental Committee on Graduate Students

Thermally-induced Deformation of Multi-layered Materials: Analytical and Engineering Formulations

by

Ching-Te Lin

Submitted to the Department of Materials Science and Engineering
on January 12, 1996, in partial fulfillment of the
requirements for the degree of
Master of Science in Materials Science and Engineering

Abstract

Analytical models are presented for thermally-induced elastoplastic deformation of bi-layer and tri-layer materials. Closed-form solutions, as functions of geometries and thermomechanical properties of layers, are derived for different phenomena associated with thermal cycling. Universal engineering diagrams for characterizing thermoelastic and thermoplastic deformation are developed. Analytical expressions for the maximum limiting curvature for a bi-layer composite with arbitrary layer thickness and material combinations are derived. The conditions governing the reversal of curvature for certain multi-layers are identified. Moreover, the criteria for the onset of plasticity at the free surfaces of bi-layer composites are derived analytically. The limiting curvatures observed experimentally have been compared with theoretical predictions for the Al(1% Si)-Si as well as Al-Al_2O_3 bi-layer models. All theoretical predictions have been shown to be in reasonable agreement with experimental observations. Finally, the theoretical predictions are applied to a number of typical layered systems which are used in thermal barrier coatings, oxidation/corrosion resistant coatings, magnetic storage devices, electronic components, and solid oxide fuel cells. The properties of selected materials of technological significance are collected and listed.

Thesis Supervisor: Subra Suresh
Title: Professor

Acknowledgments

I am grateful to my thesis supervisor, Professor Subra Suresh, for his technical guidance, support, and constant encouragement throughout the work.

Also, I would like to thank Dr. Y.L.Shen for his assistance during my experimental studies and advice on the text of my thesis.

Further, I appreciate Marc Finot for his help during my numerical analyses, Edison Chu for his suggestions on the text of the thesis, and the other members of the experimental and computational micromechanics group for their discussions, comments, and assistance.

Finally, I would like to give the thanks to my family, friends, and other people who have helped me during my work.

Contents

1 Introduction **11**

2 Problem Formulation and Background Information **14**

2.1 Problem Formulation 14

2.2 Background Information 15

2.2.1 Tri-Layer Systems 15

2.2.2 Bi-layer Systems 21

3 Elasto-plastic Deformation of Bi-layer Materials **23**

3.1 Derivation of the Maximum Normalized Curvature, $\bar{\kappa}_{max}$, during Elastic Deformation 24

3.2 The Existence of the Free Surface Yielding Phenomenon 26

3.3 Normalization of the Three Characteristic Temperatures, ΔT_1, ΔT_3, and ΔT_5 31

3.4 Normalization of the Elastic Limiting Curvature, κ_e, and the Plastic Limiting Curvature, κ_l 33

4 Elasto-plastic Deformation of Tri-layer Materials **36**

4.1 Criterion Governing the Curvature Reversal 37

4.2 Prediction of the Interface at which Plasticity Begins 38

5 Experimental Results and Numerical Check **41**

5.1 Experimental Results 41

5.1.1 Al Alloy-Si Bi-layer System 42

5.1.2 Al-Al_2O_3 Bi-layer System 44
5.1.3 SiO_2-Al Alloy-Si Tri-layer System 45
5.1.4 SiO_2-Al-Si Tri-layer System 46
5.2 Numerical Check 47
5.2.1 Bi-layer Systems 47
5.2.2 Tri-layer Systems 48

6 Applications **50**
6.1 Thermal Barrier Coatings (TBCs) 51
6.2 High Temperature Corrosion Resistant Coatings 52
6.3 Electronic Materials 53
6.4 Magnetic Storage Devices 53
6.5 Solid Oxide Fuel Cells (SOFCs) 55

7 Conclusions and Future Work **56**
7.1 Conclusions 56
7.2 Future Work 58

A TABLES **59**

B Figures **69**

List of Tables

A.1 Theoretical and Numerical Results for Two-Layer Systems 60
A.2 Theoretical and Numerical Results for Three-Layer Systems 61
A.3 Thermal Barrier Coatings 62
A.4 High Temperature Corrosion Resistant Coatings 63
A.5 Electronic Coating Systems 64
A.6 Magnetic Recording Devices 65
A.7 Solid Oxide Fuel Cells 66
A.8 Material Properties for Selected Ceramics 67
A.9 Material Properties for Selected Metals 68

List of Figures

B-1 The stress-strain response of a ductile layer. 70

B-2 The stress-strain response of a brittle layer. 71

B-3 The schematic diagram of the initiation of yielding of layer 1 at $\Delta T = \Delta T_1$. 72

B-4 The schematic diagram of full yielding of layer 1 at $\Delta T = \Delta T_3$. . . . 73

B-5 The schematic in-plane geometry of a tri-layer material. 74

B-6 The schematic in-plane geometry of a bi-layer material. 75

B-7 The normalized elastic curvature with $\bar{E}_1/\bar{E}_2$ and h_1/h_2 for bi-layer systems. 76

B-8 Schematic profile of stress distribution in a ductile layer at ΔT_5 for bi-layer systems. 77

B-9 The characteristic temperatures ΔT_1, ΔT_3, and ΔT_5 with $\bar{E}_1/\bar{E}_2$ and h_1/h_2 for bi-layer systems. 78

B-10 The evolution of normalized elastic and plastic limiting curvatures $\bar{\kappa}_e$ and $\bar{\kappa}_l$ with $\bar{E}_1/\bar{E}_2$ and h_1/h_2 for bi-layer systems. 79

B-11 The characteristic temperatures ΔT_1 and ΔT_3 with h_2/h_1 as well as h_3/h_1 for the specific system Si-Al-SiO_2. 80

B-12 One type of κ-T schematic diagram with curvature reversal. 81

B-13 Another type of κ-T schematic diagram with curvature reversal. . . . 82

B-14 One type of κ-T schematic diagram with curvature reversal (critical condition). 83

B-15 Another type of κ-T schematic diagram with curvature reversal (critical condition). 84

B-16 The κ-T diagram for the bi-layer system Al(1% Si)-Si. 85
B-17 The κ-T diagram for the bi-layer system Al-Al_2O_3. 86
B-18 The κ-T diagram for the tri-layer system Si-Al(1% Si)-SiO_2. 87
B-19 The κ-T diagram for the tri-layer system Si-Al-SiO_2. 88
B-20 The numerical results of the profiles of stress distribution in a bi-layer system with $\bar{E}_1/\bar{E}_2 = 1$ and $h_1/h_2 = 2$ at temperatures around ΔT_1. . 89
B-21 The numerical results of the profiles of stress distribution in a bi-layer system with $\bar{E}_1/\bar{E}_2 = 1$ and $h_1/h_2 = 2$ at temperatures around ΔT_5. . 90
B-22 The numerical results of the profiles of stress distribution in a bi-layer system with $\bar{E}_1/\bar{E}_2 = 10$ and $h_1/h_2 = 1$ at temperatures around ΔT_1. 91
B-23 The numerical results of the profiles of stress distribution in a bi-layer system with $\bar{E}_1/\bar{E}_2 = 10$ and $h_1/h_2 = 1$ at temperatures around ΔT_5. 92
B-24 The numerical results of the profiles of stress distribution in Si-Al-SiO_2 system with $h_2/h_1 = 1$ and $h_3/h_1 = 4$ at temperatures around ΔT_1. . 93
B-25 The numerical results of the profiles of stress distribution in Si-Al-SiO_2 system with $h_2/h_1 = 4$ and $h_3/h_1 = 1$ at temperatures around ΔT_1. . 94
B-26 The numerical results of the profiles of stress distribution in Si-Al-SiO_2 system with $h_2/h_1 = 1$ and $h_3/h_1 = 0.25$ at temperatures around ΔT_1. 95
B-27 The numerical results of the profiles of stress distribution in Si-Al-SiO_2 system with $h_2/h_1 = 0.25$ and $h_3/h_1 = 1$ at temperatures around ΔT_1. 96
B-28 The numerical results of the evolution of curvature in Si-Al-SiO_2 system with $h_2/h_1 = 1$ and $h_3/h_1 = 4$ during a cycle $\Delta T = 0°C \rightarrow 150°C \rightarrow 0°C$. 97
B-29 The numerical results of the evolution of curvature in Si-Al-SiO_2 system with $h_2/h_1 = 4$ and $h_3/h_1 = 1$ during a cycle $\Delta T = 0°C \rightarrow 150°C \rightarrow 0°C$. 98
B-30 The numerical results of the evolution of curvature in Si-Al-SiO_2 system with $h_2/h_1 = 1$ and $h_3/h_1 = 0.25$ during a cycle $\Delta T = 0°C \rightarrow 150°C \rightarrow 0°C$. 99

B-31 The numerical results of the evolution of curvature in Si-Al-SiO_2 system with $h_2/h_1 = 0.25$ and $h_3/h_1 = 1$ during a cycle $\Delta T = 0°C \rightarrow 150°C \rightarrow 0°C$. 100

Chapter 1

Introduction

Multi-layered structures are widely used in the design of mechanical, thermal, tribological, electrical, and optical systems to extend service lifetime, enhance surface strength, or improve performance of systems. However, in any type of multi-layered system, thermal residual stresses are induced because of the mismatch of thermal expansion and contraction between different layers during temperature fluctuations. The thermally-induced stresses, if high enough, may cause debonding of the interfaces, cracking and spalling in the ceramic coatings, or yielding and failure in the metallic layers.

There has been considerable progress made in the theoretical treatment that relates elastic stress and curvature [1-7] and thermally-induced elastic deformation [8-12] of multi-layered film structures. For example, as early as 1909, Stoney [1] derived Stoney's formula, which gives the relation between elastic stress and curvature in thin film systems. Recently, Freund [12] has shown that the stress distribution and curvature for a thin layer with arbitrary compositional gradation, along with general thickness variation of temperature and/or epitaxial mismatch strain, can be determined in closed form by means of elementary formulae. For general bi-layer materials with a sharp interface, Suresh *et al.* [13] derived closed-form solutions for four different characteristic temperatures at which distinct transitions of deformation behavior occur during thermal cycling. Shen and Suresh [14] extended these analytical solu-

tions to general tri-layer materials with sharp interfaces. For multi-layered materials without sharp interfaces, Giannakopoulos *et al.* [15] have also done the similar studies. Furthermore, Finot and Suresh [16] have examined the thermomechanical response of bi-layer and tri-layer materials, with or without sharp interfaces, subjected to small and large deformations during temperature fluctuations.

The current work extends the analytical studies of Suresh *et al.* [13] and Shen and Suresh [14] to examine a variety of small deformation characteristics of general bi-layer and tri-layer materials with sharp interfaces. The specific objectives of this study are:

- to develop a general framework and a series of engineering diagrams for the representation of the thermoelastic and thermoplastic deformation characteristics of multi-layered materials with applications in structural components, microelectronics, magnetic systems, and solid oxide fuel cells,
- to derive closed-form solutions for the theoretical maximum elastic curvature and the conditions governing the onset of yielding at the free surface of a general bi-layer composite,
- to obtain criteria for the occurrence of curvature reversal and the prediction of the interface location for the onset of yielding in a general tri-layer material,
- to investigate the effects of layer geometries and material properties, such as Young's modulus, thermal expansion coefficients, and yield strength, on the overall elasto-plastic response of multi-layered materials, and
- to validate the analytical formulations through comparisons with experimental results and numerical predictions.
- to analyze a number of practical multi-layered systems such as thermal barrier coatings, oxidation/corrosion resistant coatings, magnetic storage devices, solid oxide fuel cells, and electronic systems.

The thesis is arranged in the following sequence. Chapter 2 describes the analytical formulations along with the underlying assumptions for bi-layer and tri-layer materials. Chapter 3 presents the derivations of maximum normalized elastic curvature and the critical temperature, ΔT_5, for the onset of yielding at the free surface in the ductile layer in a bi-layer composite. Chapter 4 describes similar phenomena for tri-layer systems. Chapter 5 presents the experimental and the numerical results. Chapter 6 includes analyses of a number of typical multi-layered systems which are used in applications such as thermal barrier coatings, oxidation/corrosion resistant coatings, magnetic storage devices, solid oxide fuel cells, and electronic systems. The thesis concludes in chapter 7 with a summary of the findings and the suggestions for future work.

Chapter 2

Problem Formulation and Background Information

2.1 Problem Formulation

The derivation of analytical expressions for multi-layered materials are based on beam and plate theory [13]. The ductile layer, which is usually a metal layer or a relatively weaker material, is modeled as an elastic-perfectly plastic material, and the brittle layer, which is usually a ceramic layer or a relatively stronger material, is modeled as an isotropic linear-elastic material. Their uniaxial stress-strain responses are sketched schematically in Figs. *B-1* and *B-2*.

In order for continuum mechanics to be valid, the thickness of each layer are significantly larger than the characteristic microstructural dimension (e.g. grain size). The interface is assumed to be perfectly bonded at all times (no delamination). The effect of creep is not considered. In addition, the influence of heat transfer is neglected by assuming that the temperature distribution is uniform everywhere inside the system during thermal fluctuations. The edge effect, which dominates over the distance of only about one layer thickness from the free edge, is neglected in the current work.

For simplicity, the thermomechanical properties, such as thermal expansion coefficient, α, yield strength, σ_y, and Young's modulus, E, are assumed to be independent

of temperature. The procedures described in this work can be easily extended, via numerical analyses, to situations where the metallic layer exhibits isotropic hardening, where the thermomechanical properties are functions of temperature, or where heat transfer occurs across the layers. The yield strength, σ_y, is assumed to be equal both in tension and compression. Small strain deformation is assumed for the particular problem considered. No mechanical loads (forces or moments) are applied in order to keep the solutions analytically tractable; however, the procedure can be extended to include mechanical loads.

The characteristic temperature ΔT_1 is defined as the critical temperature change that causes the initiation of plastic flow in the ductile layer (Fig. *B-3*). In Fig. *B-3*, yielding commences at the interface and spreads toward layer 1 when $\Delta T = \Delta T_1$. ΔT_3 is defined as the critical temperature change at which the ductile layer becomes fully plastic (Fig. *B-4*). Figure *B-4* represents the moment at which layer 1 becomes fully plastic at $\Delta T = \Delta T_3$.

Although all the derivations are based on the assumption of a plane-stress model, they can be applied to a biaxial-stress state model by replacing Young's modulus E with the effective Young's modulus $\bar{E} = E/(1-\nu)$. Similar extensions are also possible, in appropriate situations, to plane strain and generalized plane strain models.

2.2 Background Information

In this section, analytical expressions for characteristic temperatures, ΔT_1 and ΔT_3, curvature, as well as stress distribution for bi-layer and tri-layer systems are collected and rewritten from [13] and [14].

2.2.1 Tri-Layer Systems

Figure *B-5* shows the schematic arrangement of a tri-layer system. Layer 1 is in the middle ductile layer with Young's modulus E_1, Poisson's ratio ν_1, yield strength σ_{1y}, and thermal expansion coefficient α_1. Layer 2 and Layer 3 are two outer brittle

layers with corresponding Young's moduli E_2 and E_3, Poisson's ratios ν_2 and ν_3, and thermal expansion coefficients α_2 and α_3.

The analytical expressions presented are based on [14] except that the location of the reference plane is reset to $z = 0$. In the current work, the location of the reference plane $z = 0$ is chosen to be at the interface between layers 1 and 2 instead of layers 1 and 3 [14]. In this study, only the components of stresses and strains along the longitudinal direction are important, assuming that, compared to the in-plane thicknesses h_1, h_2, and h_3, the dimension of the system along the y-axis is small and the dimension along the x-axis is large. The variation of the longitudinal strain ϵ_{xx} along the z-axis is

$$\epsilon = \epsilon_{xx} = \epsilon_0 + \kappa z \ , \tag{2.1}$$

where κ is the curvature of the beam (κ is the same everywhere in the beam) and ϵ_0, by definition, is the total strain at the interface between layer 1 and layer 2. The thermally induced elastic stresses parallel to the x-axis in the three layers are [17]

$$\begin{aligned} \sigma_1 &= \sigma_{xx}|_1 = E_1(\epsilon - \alpha_1 \Delta T) \ , \\ \sigma_2 &= \sigma_{xx}|_2 = E_2(\epsilon - \alpha_2 \Delta T) \ , \\ \sigma_3 &= \sigma_{xx}|_3 = E_3(\epsilon - \alpha_3 \Delta T) \ . \end{aligned}$$

The equations for equilibrium of longitudinal forces and moments, individually, are given by

$$\int_{-h_2}^{0} \sigma_2 dz + \int_{0}^{h_1} \sigma_1 dz + \int_{h_1}^{h_1+h_3} \sigma_3 dz = F_{\text{appl}} \ ,$$

and

$$\int_{-h_2}^{0} \sigma_2 z dz + \int_{0}^{h_1} \sigma_1 z dz + \int_{h_1}^{h_1+h_3} \sigma_3 z dz = M_{\text{appl}} \ ,$$

where F_{appl} and M_{appl} represent the applied forces and moments, respectively. Since

it is assumed that there are no external forces or moments, the applied forces and moments are zero. Therefore, the equations for equilibrium of longitudinal forces and moments prior to yielding of layer 1, individually, are given by

$$\int_{-h_2}^{0} \sigma_2 dz + \int_{0}^{h_1} \sigma_1 dz + \int_{h_1}^{h_1+h_3} \sigma_3 dz \;=\; 0\,, \tag{2.2}$$

and

$$\int_{-h_2}^{0} \sigma_2 z dz + \int_{0}^{h_1} \sigma_1 z dz + \int_{h_1}^{h_1+h_3} \sigma_3 z dz \;=\; 0\,. \tag{2.3}$$

By combining Eq. (2.1) - Eq. (2.3), ϵ_0 and κ can be obtained as

$$\epsilon_0 \;=\; \frac{C_1}{C_2}\Delta T\,,$$

and

$$\kappa \;=\; \frac{C_1 C_3 + C_2 C_4}{C_2 C_5}\Delta T\,,$$

where

$$\begin{aligned}
C_1 \;=\;& \frac{1}{12}(\alpha_1 E_1^2 h_1^4 + \alpha_2 E_2^2 h_2^4 + \alpha_3 E_3^2 h_3^4) + E_1 E_2 h_1 h_2 \left[\frac{1}{3}(\alpha_1 h_2^2 + \alpha_2 h_1^2) + \frac{1}{4}h_1 h_2(\alpha_1 + \alpha_2)\right] \\
&+ E_1 E_3 h_1 h_3 \left[\frac{1}{6}(2\alpha_1 h_3^2 - \alpha_3 h_1^2) + \frac{1}{4}h_1 h_3(\alpha_1 - \alpha_3) + \frac{1}{2}\alpha_1 h_1(h_1 + h_3)\right] \\
&+ E_2 E_3 h_2 h_3 \left[\frac{1}{3}(\alpha_2 h_3^2 + \alpha_3 h_2^2) + \alpha_2 h_1(h_1 + h_3) + \frac{1}{2}h_1 h_2(\alpha_2 + \alpha_3) + \frac{1}{4}h_2 h_3(\alpha_2 + \alpha_3)\right]\,, \\
C_2 \;=\;& \frac{1}{12}(E_1^2 h_1^4 + E_2^2 h_2^4 + E_3^2 h_3^4) + E_1 E_2 h_1 h_2 \left[\frac{1}{3}(h_2^2 + h_1^2) + \frac{1}{2}h_1 h_2\right] \\
&+ E_1 E_3 h_1 h_3 \left[\frac{1}{3}(h_1^2 + h_3^2) + \frac{1}{2}h_1 h_3\right] \\
&+ E_2 E_3 h_2 h_3 \left[\frac{1}{3}(h_2^2 + h_3^2) + \frac{1}{2}h_2 h_3 + h_1 h_2 + h_1 h_3 + h_1^2\right]\,,
\end{aligned}$$

$$C_3 = \frac{1}{2}(E_2h_2^2 - E_1h_1^2 - E_3h_3^2) - E_3h_1h_3 ,$$

$$C_4 = \frac{1}{2}(\alpha_1E_1h_1^2 + \alpha_3E_3h_3^2 - \alpha_2E_2h_2^2) + \alpha_3E_3h_1h_3 ,$$

$$C_5 = \frac{1}{3}(E_1h_1^3 + E_2h_2^3 + E_3h_3^3) + E_3h_1h_3(h_1 + h_3) .$$

Also, the stresses at the two interfaces of layer 1 before yielding are

$$\sigma_1|_{1/2} = E_1(\epsilon_0 - \alpha_1\Delta T_1) ,$$

and

$$\sigma_1|_{1/3} = E_1(\epsilon_0 + \kappa h_1 - \alpha_1\Delta T_1) .$$

The subscripts 1/2 and 1/3 refer to the interfaces between layers 1 and 2 and layers 1 and 3, respectively. If the magnitude of ΔT continues to increase up to ΔT_1, layer 1 will start to yield. For a tri-layer system, the derivation of ΔT_1 is more involved compared to the bi-layer case because there are two interfaces. It can, however, can still be derived in the following manner:
if $C_1C_3 + C_2C_4 < 0$, then

$$\sigma_1|_{1/3} = \sigma_{1y} = E_1(\epsilon_0 + \kappa h_1 - \alpha_1\Delta T_1) ,$$

and

$$\Delta T_1|_{1/3} = \frac{\sigma_{1y}}{E_1}\left(\frac{C_1}{C_2} + h_1\frac{C_1C_3 + C_2C_4}{C_2C_5} - \alpha_1\right)^{-1} ; \qquad (2.4)$$

otherwise, if $C_1C_3 + C_2C_4 > 0$, then

$$\sigma_1|_{1/2} = \sigma_{1y} = E_1(\epsilon_0 - \alpha_1\Delta T_1) ,$$

and

$$\Delta T_1|_{1/2} = \frac{\sigma_{1y}}{E_1}\left(\frac{C_1}{C_2} - \alpha_1\right)^{-1} ; \tag{2.5}$$

for the special case of $C_1C_3 + C_2C_4 = 0$,

$$\Delta T_1|_{1/2} = \Delta T_1|_{1/3} = \frac{\sigma_{1y}}{E_1}\left(\frac{C_1}{C_2} - \alpha_1\right)^{-1} .$$

That is, the entire layer 1 instantly becomes fully plastic when $\Delta T = \Delta T_1$. The critical conditions for $C_1C_3 + C_2C_4$ will be derived and discussed in detail in Chapter 3. When $\Delta T = \Delta T_1$, the elastic limiting curvature can be obtained as

$$\kappa|_{\Delta T = \Delta T_1} = \frac{C_1C_3 + C_2C_4}{C_2C_5}\Delta T_1 .$$

If ΔT keeps increasing until ΔT_3, layer 1 becomes fully yielded. Beyond ΔT_3, equilibrium of longitudinal forces and moments gives

$$\int_{-h_2}^{0} \sigma_2 dz + \int_{0}^{h_1} \sigma_{1y} dz + \int_{h_1}^{h_1+h_3} \sigma_3 dz = 0 , \tag{2.6}$$

and

$$\int_{-h_2}^{0} \sigma_2 z dz + \int_{0}^{h_1} \sigma_{1y} z dz + \int_{h_1}^{h_1+h_3} \sigma_3 z dz = 0 . \tag{2.7}$$

In the above two equations, the stresses in layer 1 equal the yield strength of layer 1 everywhere. After layer 1 fully yields,

$$\epsilon_0 = C_6 + \Delta T\frac{C_7}{C_8} - \sigma_{1y}h_1\frac{1}{C_8} ,$$

and

$$\kappa = C_6\frac{C_8}{C_9} ,$$

where

$$C_6 = \left(\Delta T\frac{C_7}{C_8} - \sigma_{1y}h_1\frac{1}{C_8} - \Delta T\frac{C_{10}}{C_{11}} - \sigma_{1y}h_2^2\frac{1}{2C_9}\right)\left[\frac{C_8C_{11}}{(C_9)^2} - 1\right]^{-1} ,$$

$$C_7 = \alpha_2E_2h_2 + \alpha_3E_3h_3 ,$$

$$C_8 = E_2h_2 + E_3h_3 ,$$

$$C_9 = \frac{1}{2}(E_2h_2^2 - E_3h_3^2) - E_3h_1h_3 ,$$

$$C_{10} = \frac{1}{2}(\alpha_2E_2h_2^2 - \alpha_3E_3h_3^2) - \alpha_3E_3h_1h_3 ,$$

$$C_{11} = \frac{1}{3}(E_2h_2^3 + E_3h_3^3) + E_3h_1h_3(h_1 + h_3) .$$

The critical temperature change, ΔT_3, can be obtained by setting either

$$\sigma_1|_{1/2} = \sigma_{1y} = E_1(\epsilon_0 - \alpha_1\Delta T_3) ,$$

or

$$\sigma_1|_{1/3} = \sigma_{1y} = E_1(\epsilon_0 + \kappa h_1 - \alpha_1\Delta T_3) ,$$

depending on which interface is the last to yield. This gives

$$\Delta T_3 = \frac{\sigma_{1y}}{E_1}\frac{C_{12} + C_{13}}{C_{14} + C_{15} + C_{16}} , \tag{2.8}$$

where

$$C_{12} = (E_1h_1 + E_2h_2 + E_3h_3)\left[\frac{1}{3}(E_2h_2^3 + E_3h_3^3) + E_3h_1h_3(h_1 + h_3)\right] ,$$

$$C_{13} = \left[\frac{1}{2}(E_2h_2^2 - E_3h_3^2) - E_3h_2h_3\right]\left[\frac{1}{2}(E_1h_1^2 + E_3h_3^2 - E_2h_2^2) + E_3h_1h_3\right] ,$$

$$C_{14} = \frac{1}{12}\left[E_2^2h_2^4(\alpha_2 - \alpha_1) + E_3^2h_3^4(\alpha_3 - \alpha_1)\right] ,$$

$$C_{15} = \frac{1}{12}E_2E_3h_2h_3\left[\alpha_2h_3(4h_3+3h_2)-2\alpha_1(2h_2^2+3h_2h_3+2h_3^2)+\alpha_3h_2(4h_2+6h_1+3h_3)\right] ,$$

$$C_{16} = \frac{1}{2}E_2E_3h_1h_2h_3\left[\alpha_2(2h_1+h_2+2h_3)-\alpha_1(h_1+h_2+h_3)\right] .$$

Also, the curvature at $\Delta T = \Delta T_3$ can be expressed as

$$\kappa|_{\Delta T=\Delta T_3} = C_6\frac{C_8}{C_9} .$$

It should be noted that the relation between curvature κ and temperature change ΔT again becomes linear once layer 1 is fully plastic.

2.2.2 Bi-layer Systems

The schematic diagram for a bi-layer system is shown in Fig. *B-6*, where layer 1 is ductile and layer 2 is brittle. The reference plane $z = 0$ is located at the interface between layer 1 and layer 2. For bi-layer systems, all analytical expressions such as ΔT_1 and κ are collected and rewritten from [13]. They can, however, also be obtained by setting $h_3 = 0$ in the tri-layer formulae given above and, they will reduce to the same equations as shown in [13].

Before layer 1 starts to yield, the longitudinal strain, ϵ_0, at the interface and the curvature, κ, can be expressed as

$$\epsilon_0 = \frac{\Delta T}{\Upsilon}\{E_1^2h_1^4\alpha_1+E_2^2h_2^4\alpha_2E_1E_2h_1h_2[4h_2^2\alpha_1+4h_1^2\alpha_2+3h_1h_2(\alpha_1+\alpha_2)]\} ,$$

and

$$\kappa = \frac{6E_1E_2(\alpha_1-\alpha_2)\Delta Th_1h_2(h_1+h_2)}{\Upsilon} , \tag{2.9}$$

where

$$\Upsilon = E_1^2h_1^4+E_2^2h_2^4+E_1E_2h_1h_2(4h_1^2+6h_1h_2+4h_2^2) .$$

The characteristic temperature ΔT_1 for yielding to start in layer 1 is

$$\Delta T_1 = \frac{\sigma_{1y}[E_1^2 h_1^4 + E_2^2 h_2^4 + E_1 E_2 h_1 h_2 (4h_1^2 + 6h_1 h_2 + 4h_2^2)]}{(\alpha_1 - \alpha_2) E_1 E_2 [E_2 h_2^4 + E_1 h_1 h_2 (4h_1^2 + 3h_1 h_2)]} . \quad (2.10)$$

The elastic limiting curvature can be obtained by substituting $\Delta T = \Delta T_1$ into Eq.(2.9), which results in

$$\kappa_e = \frac{6E_1 E_2 (\alpha_1 - \alpha_2) \Delta T_1 h_1 h_2 (h_1 + h_2)}{\Upsilon} . \quad (2.11)$$

The critical temperature change, ΔT_3, at which layer 1 becomes fully plastic is

$$\Delta T_3 = \frac{\sigma_{1y}}{(\alpha_1 - \alpha_2)} \left\{ 1 + \left(\frac{E_1}{E_2}\right) \left[4 \left(\frac{h_1}{h_2}\right) + 9 \left(\frac{h_1}{h_2}\right)^2 + 6 \left(\frac{h_1}{h_2}\right)^3 \right] \right\} , \quad (2.12)$$

and the limiting curvature is

$$\kappa_l = \frac{6\sigma_{1y}}{h_2 E_2} \left(\frac{h_1}{h_2}\right) \left(\frac{h_1}{h_2} + 1\right) . \quad (2.13)$$

It should be noted that the curvature reaches a limiting value once layer 1 is fully yielded in a bi-layer system; however, the curvature will continue to change linearly for $\Delta T > \Delta T_3$ in a tri-layer system.

Chapter 3

Elasto-plastic Deformation of Bi-layer Materials

In this chapter, the maximum elastic curvature and the temperature, ΔT_5, for the onset of yielding at the free surface are derived for a general bi-layer composite. Engineering diagrams are presented whose predictions span the thickness ratio h_1/h_2 of 10^{-3} to 10^3 in order to simulate the possible practical ranges of ceramic films on metal substrates (e.g., structural coatings) or metal films on brittle substrates (e.g., thin-film multilayers or microelectronic and magnetic applications). Similar variations are also examined for E_1/E_2 due to the fact that in multi-layered systems containing polymer and metal layers, such as magnetic devices, the ratio of the Young's moduli between polymers and metals is as low as 10^{-3} because of the very low Young's moduli of polymers.

The analytical expressions derived and figures presented are based on the following assumptions:

- All the materials properties, such as Young's modulus, E, Poisson's ratio, ν, the thermal expansion coefficient, α, and yield strength, σ_y, are constants. In other words, they are independent of the temperature, the stress and the strain level,

- The multilayers are subjected to a state of plane stress,

- Layer 1 is the ductile layer whose deformation follows an isotropic, elastic perfectly plastic behavior (rate-independent), and
- Layer 2 is the brittle layer whose deformation follows an isotropic, linear elastic behavior.

3.1 Derivation of the Maximum Normalized Curvature, $\bar{\kappa}_{max}$, during Elastic Deformation

For a bi-layer material both of whose layers comprise linear elastic materials with isotropic properties, the relation between the curvature, κ, and temperature change, ΔT, is linear, and it can be expressed as Eq. (2.9). Although there may be some pre-existing curvature due to intrinsic stresses arising from the processing procedure at initial temperature $\Delta T = 0$, Eq. (2.9) is still valid. It can also be seen from Eq. (2.9) that the curvature κ has the dimension "1/length" and is proportional to the total thickness $(h_1 + h_2)$ as well as the thermal strain $(\alpha_1 - \alpha_2)\Delta T$, which is a dimensionless number. Therefore, κ can be normalized by these two terms. The normalized κ, then, is expressed as

$$\begin{aligned} \bar{\kappa} &= \frac{\kappa(h_1 + h_2)}{\Delta T(\alpha_1 - \alpha_2)} \\ &= \frac{[6E_1E_2h_1h_2(h_1 + h_2)](h_1 + h_2)}{\Upsilon} . \end{aligned} \tag{3.1}$$

Figure *B-7* is constructed by using Eq. (3.1) with the biaxial Young's moduli $\bar{E}_1$ and $\bar{E}_2$. It can be seen that for any bi-layer composite with any combination of geometry and material properties, the trends shown in Fig. *B-7* must be followed, assuming linear elasticity holds.

In Fig. *B-7*, the contours converge from both the lower left corner (the region where the thickness and the elastic modulus of layer 2 are much greater than those of layer 1) and the upper right corner (the region where the thickness and the elastic

modulus of layer 2 are much smaller than those of layer 1) towards the center of the figure. Furthermore, the shape of the contours also changes. It starts as a curved line on both sides and ends as a straight line in the center. This straight line represents the maximum value of $\bar{\kappa}$. In order to find the maximum value of $\bar{\kappa}$ and the slope of this straight line, let

$$\frac{\partial \bar{\kappa}}{\partial E_1} = 0 .$$

Then

$$\begin{aligned}
\frac{\partial \bar{\kappa}}{\partial E_1} &= \frac{6E_2h_1h_2(h_1+h_2)^2}{\Upsilon} \\
&\quad - \frac{6E_1E_2h_1h_2(h_1+h_2)^2(2E_1h_1^4+4E_2h_1^3h_2+6E_2h_1^2h_2^2+4E_2h_1h_2^3)}{\Upsilon^2} \\
&= [6E_2h_1h_2(h_1+h_2)^2] \\
&\quad \left[\frac{1}{\Upsilon} - \frac{E_1(2E_1h_1^4+4E_2h_1^3h_2+6E_2h_1^2h_2^2+4E_2h_1h_2^3)}{\Upsilon^2}\right] .
\end{aligned}$$

Since $[6E_2h_1h_2(h_1+h_2)^2]$ is always either positive or zero, the necessary condition for $\partial\bar{\kappa}/\partial E_1 = 0$ is

$$\left[\frac{1}{\Upsilon} - \frac{E_1(2E_1h_1^4+4E_2h_1^3h_2+6E_2h_1^2h_2^2+4E_2h_1h_2^3)}{\Upsilon^2}\right] = 0 .$$

That is,

$$E_1^2h_1^4 - E_2^2h_2^4 = 0 ,$$

which leads to

$$\frac{h_1}{h_2} = \left(\frac{E_2}{E_1}\right)^{1/2} .$$

After substituting this equation into Eq. (3.1), Eq. (3.1) becomes

$$\bar{\kappa}_{max} = \frac{E_1^2 6h_1h_2(h_1+h_2)^2(\frac{h_1}{h_2})^2}{E_1^2[h_1^4+(\frac{h_1}{h_2})^4h_2^4+4(\frac{h_1}{h_2})^2h_1^3h_2+6(\frac{h_1}{h_2})^2h_1^2h_2^2+4(\frac{h_1}{h_2})^2h_1h_2^3]}$$

$$= \frac{6[2h_1^4h_2^4 + h_1^3h_2^3(h_1^2 + h_2^2)]}{4[2h_1^4h_2^4 + h_1^3h_2^3(h_1^2 + h_2^2)]}$$

$$= \frac{3}{2} .$$

Therefore, the maximum value of $\bar{\kappa}$ is 1.5, which occurs at $h_1/h_2 = (E_2/E_1)^{1/2}$. The slope of the straight line is -2. Since E_1, E_2, h_1, and h_2 are mutually independent, the same result can also be obtained by taking $\partial\bar{\kappa}/\partial E_2$, $\partial\bar{\kappa}/\partial h_1$, or $\partial\bar{\kappa}/\partial h_2$. For example, by taking $\partial\bar{\kappa}/\partial h_1$,

$$\frac{\partial\bar{\kappa}}{\partial h_1} = \frac{6E_1E_2h_2(h_1 + h_2)(3h_1 + h_2)}{\Upsilon}$$

$$- \frac{6E_1E_2h_1h_2(h_1 + h_2)^2[4E_1^2h_1^3 + E_1E_2h_2(12h_1^2 + 12h_1h_2 + 4h_2^2)]}{\Upsilon^2}$$

$$= \frac{[6E_1E_2h_2(h_1 + h_2)^2]}{\Upsilon^2}(E_1h_1^2 - E_2h_2^2)[E_1h_1^2(h_1 + 3h_2) + E_2h_2^2(3h_1 + h_2)] .$$

Since the only condition that can satisfy $\partial\bar{\kappa}/\partial h_1 = 0$ is $(E_1h_1^2 - E_2h_2^2) = 0$, the same result, $h_1/h_2 = (E_2/E_1)^{1/2}$, is obtained. It should be noted that the condition governing the occurrence of $\bar{\kappa}_{max}$ depends only on the layer thickness and Young's modulus and is independent of the yield strength and the thermal expansion coefficient.

3.2 The Existence of the Free Surface Yielding Phenomenon

Although plasticity always starts at the interface in bi-layer composites, it is not necessary for plasticity to spread out from the interface to the free surface monotonically in a ductile layer. For certain combinations of geometries and materials properties, there exists another characteristic temperature, ΔT_5. ΔT_5 represents the temperature at which the free surface of a ductile layer starts to yield before the plastic zone spreading outward from the interface reaches the free surface (Fig. *B-8*), and its value is between ΔT_1 and ΔT_3.

In Fig. *B-8*, the plastic zone spreads from the interface toward layer 1 and, at the same time, the magnitude of the stress at the surface keeps increasing. When ΔT reaches ΔT_5, this stress equals the yield stress and, therefore, the free surface starts to yield. At $\Delta T = \Delta T_5$, it is assumed that the size of the plastic zone has a thickness h.

When a ductile layer starts to yield at the free surface, the equation for equilibrium of the longitudinal forces becomes

$$\int_{-h_2}^{0} \sigma_2 dz + \int_{0}^{h} \sigma_{1y} dz + \int_{h}^{h_1} \sigma_1 dz = 0 \ , \tag{3.2}$$

and the equation for equilibrium of the moments can be expressed as

$$\int_{-h_2}^{0} \sigma_2 z dz + \int_{0}^{h} \sigma_{1y} z dz + \int_{h}^{h_1} \sigma_1 z dz = 0 \ . \tag{3.3}$$

Furthermore, there are two constraints which must be satisfied because of continuity at the elastic-plastic boundary in layer 1. They are

$$\sigma_1|_{z=h} \ = \ \sigma_{1y} \ , \tag{3.4}$$

and

$$\sigma_1|_{z=h_1} \ = \ -\sigma_{1y} \ , \tag{3.5}$$

where h is the thickness of the plastic zone in layer 1 (Fig. *B-8*) and σ_{1y} is either the tensile or compressive yield strength depending on the sign of ΔT. Equation (3.4) is the necessary condition for stresses to be continuous at a distance h from interface. On the other hand, Eq. (3.5) must be satisfied if ΔT_5 exists.

After rearranging Eq. (3.2) - Eq. (3.5),

$$C_1' \epsilon_0 + C_2' \kappa + C_3' \Delta T \ = \ -\sigma_{1y} h \ , \tag{3.6}$$

$$C_2'\epsilon_0 + C_4'\kappa + C_5'\Delta T = -\frac{1}{2}\sigma_{1y}h^2 , \tag{3.7}$$

$$\epsilon_0 + h\kappa - \alpha_1\Delta T = \frac{\sigma_{1y}}{E_1} , \tag{3.8}$$

$$\epsilon_0 + h_2\kappa - \alpha_1\Delta T = -\frac{\sigma_{1y}}{E_1} , \tag{3.9}$$

where

$$\begin{aligned}
C_1' &= E_1(h_1 - h) + E_2h_2 , \\
C_2' &= \frac{1}{2}E_1(h_1^2 - h^2) - \frac{1}{2}E_2h_2^2 , \\
C_3' &= -E_1\alpha_1(h_1 - h) - E_2\alpha_2h_2 , \\
C_4' &= \frac{1}{3}E_1(h_1^3 - h^3) + \frac{1}{3}E_2h_2^3 , \\
C_5' &= -\frac{1}{2}E_1\alpha_1(h_1^2 - h^2) + \frac{1}{2}E_2\alpha_2h_2^2 .
\end{aligned}$$

By using Cramer's rule to solve Eq. (3.6) - Eq. (3.8), ϵ_0, κ, and ΔT can be expressed as

$$\epsilon_0 = \frac{\sigma_{1y}}{\Lambda}\left[h(\alpha_1C_4' - h^2C_3') + \frac{1}{E_1}(C_2'C_5' - C_3'C_4') + h^2\left(C_5' - \frac{1}{2}\alpha_1C_2'\right)\right], \tag{3.10}$$

$$\kappa = \frac{\sigma_{1y}}{\Lambda}\left[\frac{1}{E_1}(C_2'C_3' - C_1'C_5') + \frac{1}{2}h^2(C_3' + \alpha_1C_1') - h(C_5' + \alpha_1C_2')\right] , \tag{3.11}$$

$$\Delta T = \frac{\sigma_{1y}}{\Lambda}\left[\frac{1}{E_1}(C_1'C_4' - C_2'^2) + \frac{1}{2}h(h^2C_1' - 3hC_2' + 2C_4')\right] , \tag{3.12}$$

where Λ is the determinant of the coefficients of Eq. (3.6) - Eq. (3.8), and is expressed as

$$\Lambda = \begin{vmatrix} C_1' & C_2' & C_3' \\ C_2' & C_4' & C_5' \\ 1 & h & -\alpha_2 \end{vmatrix}$$

$$= h(C_2'C_3' - C_1'C_5') + (C_2'C_5' - C_3'C_4') - \alpha_1(C_1'C_4' - C_2'^2) \ .$$

By adding Eq. (3.8) and Eq. (3.9),

$$2\epsilon_0 + (h_1 + h)\kappa - 2\alpha_1\Delta T = 0 \ . \tag{3.13}$$

After substituting Eq. (3.10) - Eq. (3.12) into Eq. (3.13) and rearranging them, Eq. (3.13) becomes

$$h^3 + Ph^2 + Qh + S = 0 \ , \tag{3.14}$$

where

$$\begin{aligned} P &= \frac{3}{2}h_2 \ , \\ Q &= -\frac{3}{2}h_1(h_1 + h_2) \ , \\ S &= \frac{1}{2}(Yh_2^3 + h_1^3) \ , \\ Y &= \frac{E_2}{E_1} \ . \end{aligned}$$

Letting $h = \chi - (P/3)$ and substituting it into Eq. (3.14) , Eq. (3.14) becomes

$$\chi^3 + a\chi + b = 0 \ , \tag{3.15}$$

where

$$\begin{aligned} a &= \frac{1}{3}(3Q - P^2) \\ &= -\frac{3}{4}[(h_1 + h_2)^2 + h_1^2] \ , \\ b &= \frac{1}{27}(2P^3 - 9PQ + 27S) \ , \\ &= \frac{1}{4}(h_1 + h_2)^3 + \frac{1}{4}h_1^3 + \frac{1}{2}Yh_2^3 \ . \end{aligned}$$

By solving Eq. (3.15), three real roots of χ can be obtained as

$$\begin{aligned} \chi_i &= -2\frac{b}{|b|}(-\frac{a}{3})^{1/2}\cos(\frac{\phi}{3}+120°i)\ , \\ &= -[(h_1+h_2)^2+h_1^2]^{1/2}\cos(\frac{\phi}{3}+120°i)\ ,\quad \mathrm{i}=0,1,2 \end{aligned} \tag{3.16}$$

where

$$\cos\phi = \left[\frac{b^2}{4}\left(-\frac{27}{a^3}\right)\right]^{1/2}\ .$$

By substituting Eq. (3.16) into $h=\chi-(P/3)$ and then using Eq. (3.12), three values of ΔT_5 can be obtained as

$$\begin{aligned} \Delta T_5^i &= \frac{-1}{(\alpha_1-\alpha_2)}\frac{\sigma_{1y}}{E_1}\left\{1+\right. \\ &\left.\frac{12uv^2\chi_i'^3-24u^2v^2\chi_i'^2+6[4uv(u+1)+3u^3v^2]\chi_i'+4uv(4-3u^2)}{12v\chi_i'^3+12v(1-u)\chi_i'^2-18uv(u+2)\chi_i'+[27u^2v(1+u)+4]}\right\}, \end{aligned} \tag{3.17}$$

where

$$\begin{aligned} \chi_i' &= -[(u+1)^2+u^2]^{1/2}\cos(\frac{\phi}{3}+120°i)\ , \\ u &= \frac{h_1}{h_2}\ , \\ v &= \frac{E_1}{E_2}\ . \end{aligned}$$

The condition necessary for ΔT_5 to exist can be determined by setting the cubic equation

$$\frac{b^2}{4}+\frac{a^3}{27}\le 0\ . \tag{3.18}$$

By rearranging Eq. (3.18), it can be shown that ΔT_5 will exist as long as the equation,

$$\frac{E_1}{E_2} \ge \left\{\left[2\left(\frac{h_1}{h_2}\right)+1\right]\left[\left(\frac{h_1}{h_2}\right)^2+\left(\frac{h_1}{h_2}\right)+1\right]+\left\{\left[2\left(\frac{h_1}{h_2}\right)+1\right]^2\left[\left(\frac{h_1}{h_2}\right)^2+\left(\frac{h_1}{h_2}\right)+1\right]^2\right.\right.$$

$$+4\left[\left(\frac{h_1}{h_2}\right)^2+\left(\frac{h_1}{h_2}\right)\right]^2\left[\left(\frac{h_1}{h_2}\right)^2+\left(\frac{h_1}{h_2}\right)+\frac{3}{4}\right]\Bigg\}^{1/2}\Bigg\}\cdot$$

$$\left\{2\left[\left(\frac{h_1}{h_2}\right)^2+\left(\frac{h_1}{h_2}\right)\right]^2\left[\left(\frac{h_1}{h_2}\right)^2+\left(\frac{h_1}{h_2}\right)+\frac{3}{4}\right]\right\}^{-1} \quad ,$$

is satisfied. It can be seen from the above equation that although the value of ΔT_5 is dependent on the layer thickness, Young's modulus, yield strength, and of the thermal expansion coefficient, the condition governing the occurrence of free surface yielding in a ductile layer depends only on the layer thickness and Young's modulus. In other words, they are independent of yield strength and the thermal expansion coefficient.

It should also be noted that ΔT_5 always appears in pairs. One is the temperature at which the free surface of a ductile layer starts to yield, and the other one is the temperature at which relaxation of yielding at the free surface of the ductile layer starts. Therefore, only one root of Eq. (3.17) is trivial. Moreover, for the condition $(b^2/4)+(a^3/27)<0$, the two values of ΔT_5 are not equal. That is, the temperature for yielding at the free surface and the temperature for relaxation of yielding at the free surface are different. However, for the condition $(b^2/4)+(a^3/27)=0$, the two values of ΔT_5 are equal. In other words, as soon as yielding starts at the free surface, relaxation of yielding at the free surface will start.

3.3 Normalization of the Three Characteristic Temperatures, ΔT_1, ΔT_3, and ΔT_5

Although the characteristic temperatures ΔT_1, ΔT_3, and ΔT_5 are dependent on properties of materials and geometries, all of them can be expressed in a nondimensional form. For instance, Eq. (2.10) is the analytical solution of ΔT_1, and is proportional

to $1/(\alpha_1 - \alpha_2)$ and σ_{1y}/E_1. Therefore, ΔT_1 can be normalized as

$$\begin{aligned}\Delta\bar{T}_1 &= \frac{\Delta T_1(\alpha_1 - \alpha_2)}{(\sigma_{1y}/E_1)} \\ &= \frac{[E_1^2 h_1^4 + E_2^2 h_2^4 + E_1 E_2 h_1 h_2 (4h_1^2 + 6h_1 h_2 + 4h_2^2)]}{E_2[E_2 h_2^4 + E_1 h_1 h_2 (4h_1^2 + 3h_1 h_2)]} .\end{aligned}$$

By using the same argument, ΔT_3 and ΔT_5 can also be obtained as

$$\begin{aligned}\Delta\bar{T}_3 &= \frac{\Delta T_3(\alpha_1 - \alpha_2)}{(\sigma_{1y}/E_1)} \\ &= \left\{1 + \left(\frac{E_1}{E_2}\right)\left[4\left(\frac{h_1}{h_2}\right) + 9\left(\frac{h_1}{h_2}\right)^2 + 6\left(\frac{h_1}{h_2}\right)^3\right]\right\} ;\end{aligned}$$

$$\begin{aligned}\Delta\bar{T}_5 &= \frac{\Delta T_5(\alpha_1 - \alpha_2)}{(\sigma_{1y}/E_1)} \\ &= 1 + \left\{12\left(\frac{h_1}{h_2}\right)\left(\frac{E_1}{E_2}\right)^2 \chi'^3 - 24\left(\frac{h_1}{h_2}\right)^2\left(\frac{E_1}{E_2}\right)^2 \chi'^2\right. \\ &\quad +6\left\{4\left(\frac{h_1}{h_2}\right)\left(\frac{E_1}{E_2}\right)\left[\left(\frac{h_1}{h_2}\right) + 1\right] + 3\left(\frac{h_1}{h_2}\right)^3\left(\frac{E_1}{E_2}\right)^2\right\}\chi' \\ &\quad \left.+4\left(\frac{h_1}{h_2}\right)\left(\frac{E_1}{E_2}\right)\left[4 - 3\left(\frac{h_1}{h_2}\right)^2\right]\right\} \cdot \\ &\quad \left\{12\left(\frac{E_1}{E_2}\right)\chi'^3 + 12\left(\frac{E_1}{E_2}\right)\left[1 - \left(\frac{h_1}{h_2}\right)\right]\chi'^2 - 18\left(\frac{h_1}{h_2}\right)\left(\frac{E_1}{E_2}\right)\left[\left(\frac{h_1}{h_2}\right) + 2\right]\chi'\right. \\ &\quad \left.+\left\{27\left(\frac{h_1}{h_2}\right)^2\left(\frac{E_1}{E_2}\right)\left[1 + \left(\frac{h_1}{h_2}\right)\right] + 4\right\}\right\}^{-1} .\end{aligned}$$

Figure *B-9* is presented by plotting $\Delta\bar{T}_1$, $\Delta\bar{T}_3$, and $\Delta\bar{T}_5$ as functions of the biaxial Young's modulus ratio, $\bar{E}_1/\bar{E}_2$ and the thickness ratio, h_1/h_2. In addition, only the

ΔT_5 that represents the temperature at which the onset of yielding at the free surface of layer 1 occurs is shown.

In Fig. *B-9*, the curves for $\Delta\bar{T}_1$ and $\Delta\bar{T}_3$ are almost overlapping and their values are very small in the lower left corner of the plot. This is because, in the lower left region, a ductile layer has much smaller thickness (i.e., the bi-layer system is a thin ductile film on a thick brittle substrate) and Young's modulus. Therefore, once it starts to yield, the entire layer instantaneously becomes fully plastic. On the other hand, as the thickness and Young's modulus of the ductile layer increase (toward the top right corner), the ductile layer becomes stronger (i.e., it resists plastic deformation); hence, the values of ΔT_1 and ΔT_3 and the curves of constant ΔT_1 and ΔT_3 move farther apart.

Another point to be addressed is that ΔT_5 appears only if the thickness and/or Young's modulus of a ductile layer are large enough compared to those of a brittle layer as shown in Fig. *B-9*. When a ductile layer is stiff, the stress distribution across it will be compressive at one surface and tensile at the other surface. Therefore, although the final stresses have the same magnitude and sign across the entire layer (either equal to the compressive or the tensile yield strength), the free surface will have a yield stress of the opposite sign compared to the yield stress of the interface at a certain temperature range. Also, on the line that separates the regions with and without ΔT_5, the two values of ΔT_5 are equal. In other words, as soon as the stress at the free surface of a ductile layer reaches the yield stress, this stress will decrease.

3.4 Normalization of the Elastic Limiting Curvature, κ_e, and the Plastic Limiting Curvature, κ_l

Equation (2.11) represents the elastic limiting curvature of a bi-layer system when $\Delta T = \Delta T_1$. This equation can also be expressed, after substituting Eq. (2.10) and

Υ into it, as

$$\kappa_e = \frac{6\sigma_{1y}h_1h_2(h_1+h_2)}{E_2{h_2}^4 + E_1h_1h_2(4{h_1}^2 + 3h_1h_2)} .$$

The above equation can then be normalized by multiplying by the total thickness, $(h_1 + h_2)$, and by dividing by σ_{1y}/E_1. Therefore, the normalized elastic limiting curvature, $\bar{\kappa}_e$, can be obtained as

$$\begin{aligned}\bar{\kappa}_e &= \frac{\kappa_e(h_1+h_2)}{(\sigma_{1y}/E_1)} \\ &= \frac{E_1}{E_2}\frac{(h_1+h_2)}{h_2}\left[6\left(\frac{h_1}{h_2}\right)^2 + 6\left(\frac{h_1}{h_2}\right)\right]\left\{1+\left(\frac{E_1}{E_2}\right)\left(\frac{h_1}{h_2}\right)^2\left[4\left(\frac{h_1}{h_2}\right)+3\right]\right\}^{-1} ,\end{aligned} \quad (3.19)$$

which is a function of h_1, h_2, E_1, and E_2 only. Equation (2.13) represents the plastic limiting curvature of a bi-layer system when $\Delta T = \Delta T_3$. This equation can also be normalized by multiplying by the total thickness, $(h_1 + h_2)$, and dividing by σ_{1y}/E_1 to get the normalized form similar to that of Eq. (3.19). The normalized plastic limiting curvature, $\bar{\kappa}_l$, can then be expressed as

$$\begin{aligned}\bar{\kappa}_l &= \frac{\kappa_l(h_1+h_2)}{(\sigma_{1y}/E_1)} \\ &= \frac{E_1}{E_2}\frac{(h_1+h_2)}{h_2}\left[6\left(\frac{h_1}{h_2}\right)^2 + 6\left(\frac{h_1}{h_2}\right)\right] ,\end{aligned} \quad (3.20)$$

which also is a function of h_1, h_2, E_1, and E_2 only.

It should be noted that although Eq. (3.19) and Eq. (3.20) are similar to Eq. (3.1), Eq. (3.1) is normalized by the total thickness, $(h_1 + h_2)$, and the total thermal strain, $(\Delta T \cdot \Delta\alpha)$. On the other hand, Eq. (3.19) and Eq. (3.20) are normalized by the total thickness, $(h_1 + h_2)$, and the yield-strength to Young's-modulus ratio, (σ_{1y}/E_1).

Figure *B-10* represents the evolution of the two normalized limiting curvatures, $\bar{\kappa}_e$ and $\bar{\kappa}_l$, with respect to the thickness ratio, h_1/h_2, and the biaxial Young's modulus ratio, $\bar{E}_1/\bar{E}_2$. It can be seen that the contours of $\bar{\kappa}_e$ and $\bar{\kappa}_l$ converge, and their values

are small when the thickness and Young's modulus of a ductile layer are much smaller than those of a brittle layer. This is due to the fact that a ductile layer has a much smaller thickness (i.e., the bi-layer system is a thin ductile film on a thick brittle substrate) and a much smaller Young's modulus in the lower left region. Therefore, once it starts to yield, the entire layer instantaneously becomes fully plastic. On the other hand, as the thickness and Young's modulus of a ductile layer increase (toward the top right corner), the ductile layer becomes stiffer (i.e., it resists plastic deformation). Hence, the contours of constant $\bar{\kappa}_e$ and $\bar{\kappa}_l$ move further apart.

Chapter 4

Elasto-plastic Deformation of Tri-layer Materials

In this chapter, two specific cases of elastoplastic deformation in tri-layer systems are examined. Since problems can potentially involve a large number of variables in tri-layer systems, one specific system, the silicon-aluminum-silica tri-layer composite, is selected for analyses because of its wide use in electronic applications. In this system, layer 1 is aluminum which represents a ductile layer, and silicon and silica represent the outer brittle layers 2 and 3, respectively.

Since materials properties are specified once a certain system is chosen, the only variables are the layer thicknesses. These can be presented as two relative thickness ratios, h_2/h_1 and h_3/h_1. Although the thickness of a top coating or a passivation layer is comparable to the thickness of a bond coating or a intermediate layer in most coating systems, the two axes, h_2/h_1 and h_3/h_1, of Fig. *B-11* still extend from 10^{-3} to 10^3 to generalize the purpose of the figure.

In this chapter, all the analytical expressions derived and figures presented are based on the assumptions discussed in the previous chapter.

4.1 Criterion Governing the Curvature Reversal

As seen in the preceding chapters, the evolution of curvature can be divided into three stages for a bi-layer system. The curvature changes linearly with ΔT before ΔT_1, then changes nonlinearly with ΔT between ΔT_1 and ΔT_3, and finally ends with a limiting curvature when ΔT goes beyond ΔT_3. For a tri-layer system, the first two stages are similar; however, there is no limiting curvature once ΔT goes beyond ΔT_3. Instead, the curvature changes linearly with ΔT again. This is due to the fact that once the ductile layer becomes fully plastic in a bi-layer system, it applies no constraints to the brittle layer; on the other hand, in a tri-layer system, although the ductile layer is fully plastic, the outer two brittle layers constrain one another. Therefore, the curvature keeps changing with temperature.

This curvature change in tri-layer systems present an additional phenomenon which is not seen in bi-layer systems (if materials properties in bi-layer systems are independent of temperature) – curvature reversal (Fig. *B-12* - Fig. *B-15*). In tri-layer systems, this phenomenon can occur even for monotonic variations in temperature and even when the properties of all layers do not vary with temperature. Here the curvature reversal phenomenon is solely a consequence of the evolution of plastic flow. The closed-form solutions of the critical conditions which govern the occurrence of curvature reversal will be derived later in this chapter.

Figures *B-12* and *B-13* schematically represent the curvature reversal phenomenon. They indicate that the slope of the curvature, under certain combinations of geometries and properties of materials, will change its sign when the ductile layer is fully plastic. Figures *B-14* and *B-15* represent two critical conditions. In these two figures, it can be seen that the curvature remains zero before the ductile layer becomes fully plastic. Therefore, the critical condition for systems having or not having curvature reversal can be obtained by having the elastic curvature, κ, be equal to zero. That is,

$$\kappa = \Delta T \frac{C_1 C_3 + C_2 C_4}{C_2 C_5} = 0 \ .$$

The above equation can then be expressed explicitly as

$$\Delta\alpha_{32}\left(\frac{E_2}{E_1}\right)\left(\frac{E_3}{E_1}\right)\left(\frac{h_2}{h_1}\right)\left(\frac{h_3}{h_1}\right)\left(2+\frac{h_2}{h_1}+\frac{h_3}{h_1}\right) = \Delta\alpha_{21}\left(\frac{E_2}{E_1}\right)\left(\frac{h_2}{h_1}\right)\left(1+\frac{h_2}{h_1}\right)+ \Delta\alpha_{13}\left(\frac{E_3}{E_1}\right)\left(\frac{h_3}{h_1}\right)\left(1+\frac{h_3}{h_1}\right), \quad (4.1)$$

where

$$\Delta\alpha_{21} = (\alpha_2 - \alpha_1)\ ,\ \Delta\alpha_{13} = (\alpha_1 - \alpha_3)\ ,\ \Delta\alpha_{32} = (\alpha_3 - \alpha_2)\ .$$

Equation (4.1) is dependent on relative thickness, relative Young's Moduli, and difference of thermal expansion coefficients, but independent of the yield strength.

4.2 Prediction of the Interface at which Plasticity Begins

For bi-layer systems, yielding always initiates at the interface. For tri-layer systems, there are two interfaces, and, therefore, it is necessary to find a closed-form solution to predict analytically at which interface of a ductile layer yielding initiates.

In most systems, the thermal expansion coefficient of a ductile layer is larger than that of the two brittle layers. Therefore, during heating, the maximum stress in a ductile layer will be compressive regardless of at which interface it starts to yield. The condition to initiate yielding in the ductile layer at the interface between layers 1 and 3 can be derived as follows. Before layer 1 yields, the stress in layer 1 at the interface between layers 1 and 2 can be expressed as

$$\sigma_1|_{1/2} = E_1(\epsilon_0 - \alpha_1\Delta T)\ .$$

Also, the stress in layer 1 at the interface between layers 1 and 3 can be expressed as

$$\sigma_1|_{1/3} = E_1(\epsilon_0 + \kappa h_1 - \alpha_1\Delta T)\ .$$

Therefore, the condition for yielding commencing at the interface between layers 1 and 3 is

$$\begin{aligned} \sigma_1|_{1/3} - \sigma_1|_{1/2} &= E_1(\epsilon_0 + \kappa h_1 - \alpha_1 \Delta T) - E_1(\epsilon_0 - \alpha_1 \Delta T) \ , \\ &= E_1 h_1 \kappa \leq 0 \ . \end{aligned} \tag{4.2}$$

Since E_1 and h_1 are both positive, Eq. (4.2) becomes

$$\kappa = \Delta T \frac{C_1 C_3 + C_2 C_4}{C_2 C_5} \leq 0 \ .$$

In addition, because $C_2 C_5$ is always positive and ΔT, by definition, is positive during heating, the necessary condition for yielding commencing at the interface between layers 1 and 3 becomes

$$C_1 C_3 + C_2 C_4 \leq 0 \ ,$$

and therefore, the critical condition is

$$C_1 C_3 + C_2 C_4 = 0 \ .$$

The above equation can be further simplified to Eq. (4.1). That is, the critical condition for the occurrence of curvature reversal is the same as the critical condition for identifying the interface at which yielding initiates (The reason will be explained later in this chapter.) Therefore, this criterion is also independent of yield strength. For cooling, the same equation can be obtained by similar arguments by taking $\Delta T < 0$.

In Fig. *B-11*, a solid curve, represents Eq. (4.1), extends from the lower left corner to the upper right corner and separates the plot into two parts. The upper half region is where the curvature will not reverse and the yielding will commence at the interface between layers 1 and 3. The lower half portion then is the region where the curvature will reverse and the yielding will initiate at the interface between layers 1 and 2. This can be explained as follows: If yielding starts at the interface between layers 1 and

3, after layer 1 is fully yielded, the curvature will continue to increase because the direction of curvature increase has the same sign as if only layers 2 and 3 were present. However, if the yielding commences at the other interface, the direction will reverse because it is not the same as if only layers 2 and 3 were present. It is also interesting to look at this solid curve. On this solid curve, the curvature is zero everywhere before ΔT reaches ΔT_3, and ΔT_1 is equal to ΔT_3. In other words, the entire ductile layer yields at the same time. Moreover, the contours of ΔT_1 and ΔT_3 converge just as they do in the bi-layer case if the thicknesses of layers 2 and/or 3 are much larger than that of layer 1.

Chapter 5

Experimental Results and Numerical Check

In this chapter, experimental measurements of limiting curvatures corresponding to full plasticity in bi-layer composites and to the curvature reversal phenomenon in tri-layer systems are reported for selected model systems. These results are compared with theoretical predictions. A laser scanning technique employed previously [18,19] was adopted to examine the evolution of curvature κ with temperature. In addition, numerical analyses are introduced to verify the analytical formulae derived in chapters 3 and 4 which determine ΔT_5 in a bi-layer system and curvature reversal and the first interface to yield in a tri-layer system. MultiTherm [20][21], a general purpose software developed for numerically estimating the thermomechanical behavior of multi-layered materials, is used for the numerical check.

5.1 Experimental Results

In this section, experimental measurements of limiting curvatures corresponding to full plasticity in bi-layer composites and to the curvature reversal phenomenon in tri-layer systems are reported for selected model systems. These results are compared with theoretical predictions. To examine the evolution of curvature κ with temperature, a laser scanning technique employed previously [18,19] was adopted.

The system used is the TENCOR FLX2320 model (Tencor Instruments, Mountain View, CA) which is a thin-film stress measurement instrument. It measures changes in the radius of the curvature of a multi-layered composite using a laser scanning technique and is capable of providing measurements during *in-situ* heating and cooling over a temperature range from -150°C to 500°C. Due to the fact that there is no sharp transition from elasticity to plasticity in any model system, the characteristic temperatures, ΔT_1 and ΔT_3, obtained from experiments are not well defined, but can be estimated to a reasonable degree of approximation.

5.1.1 Al Alloy-Si Bi-layer System

The Al alloy-Si bi-layer wafer specimen was prepared at MIT Lincoln Laboratory (Lexington, MA). The silicon substrate, which has (100) orientation, has a thickness of 620 μm and a diameter of 10 cm. The 1 μm thick Al-1% Si film was deposited by sputtering on to the oxidized substrate. In order to avoid interdiffusion between layers, the substrate was first oxidized to have a 185 Å thick oxide layer. This very thin layer of SiO_2 is known to have an insufficient effect on the thermomechanical response. The specimen was then subjected to thermal cycling to measure the curvature.

Figure *B-16* presents the curvature, κ, as a function of the temperature, T, for a saturated cycle (i.e., the shape of the κ-T diagram for a complete cycle does not change with further cycling) for thermally cycling the specimen with a temperature range between 25°C and 440°C at a 10°C/min heating and cooling rate step. After the first cycle, the curvature became saturated due to microstructural stabilization.

Although in thin film structures, the thin film is supposed to yield instantaneously (i.e., $\Delta T_1 = \Delta T_3$,) Fig. *B-16* does not show a sharp transition in curvature evolution. This is because the thin film is not an elastic-perfectly plastic material. Therefore in this figure, κ, during heating, varies linearly with T from 25°C to 150°C and nonlinearly with T between 150°C and 250°C. Beyond 250°C, κ retains constant until 375°C and then increases until the end of the heating cycle. This increase in curvature is because the yield strength of the metal layer is temperature-dependent

(i.e., σ_y decreases with increasing temperature.) In addition, since the specimen already experienced plastic deformation when it was cooled down from the processing temperature to room temperature before being subjected to thermal cycling, the corresponding temperature change is, according to the definition of Suresh *et al.* [13], ΔT_2 and ΔT_4. In their work, ΔT_2 is the temperature at which the complete suppression of reversed plastic flow in the ductile layer occurs and its value is equal to twice the value of ΔT_1, when the magnitudes of the yield strength are assumed to be equal for tension and compression. ΔT_4, whose value is twice the value of ΔT_3, is the temperature at which yielding in the ductile layer becomes fully reversed. In Fig. *B-16*, by extrapolating the curve, the critical temperature change can be obtained as 175°C (T_h) and 110°C (T_c) for the heating and cooling cycles, respectively. Therefore, ΔT_1 (ΔT_3) is 87.5°C and 55°C for the heating and cooling cycles, respectively. The difference between these two values results from the effect of yield strength as a function of temperature.

The theoretical values of ΔT_1 and ΔT_3 can also be obtained by using Eqs. (2.10) and (2.12), respectively. Nevertheless, it should be noted that the properties of thin films are very different from the properties of bulk materials (i.e., properties of thin films are strongly dependent on the layer thickness), especially for yield strength. For the 1 μm thick Al film, if the yield strength is 100 MPa, 125 MPa, 150 MPa, or 175 MPa, ΔT_1 (ΔT_3) will be 49°C, 62°C, 74°C, or 87°C, respectively. By comparing the theoretical values with the experimental values, it is reasonable to assume that the Al thin film has an approximate yield strength of 175 MPa (see also Venkatraman *et al.* [22].) at low temperatures and 135 MPa at high temperatures. The difference between the experimental and theoretical results may be due to the changes in microstructure and the effects of strain hardening and yield strength as a function of temperature. In addition, it should be noted that Eqs. (2.10) and (2.12) can not only give the values of ΔT_1 and ΔT_3, but can also predict the approximate yield strength of thin films.

5.1.2 Al-Al_2O_3 Bi-layer System

The Al-Al2O_3 bi-layer specimen had an in-plane dimension of 25 mm x 25 mm and was made by diffusion bonding a 1 mm thick, polycrystalline alumina layer to a 1 mm thick, polycrystalline 1100-O aluminum layer at 500°C. For the thermal cycling condition examined in this case, the interface remained perfectly bonded and no failure was observed [14].

Figure *B-17* shows the evolution of the curvature, κ, as a function of the temperature, T. The specimen was subjected to a 0°C-200°C-0°C thermal cycle with a 10°C/min heating and cooling rate step. By examining Fig. *B-17*, it can be seen that κ varies linearly with T from 0°C to 70°C, then varies nonlinearly with T between 70°C and 180°C. Beyond 80°C, it retains constant until the end of the heating cycle. During cooling, κ varies linearly with T from 200°C to 130°C, then varies nonlinearly with T between 130°C and 10°C, and retains the same value below 10°C. Accordingly, ΔT_1 and ΔT_3, are 35°C and 90°C, respectively, during the heating cycle, and they are 35°C and 95°C, respectively, during the cooling cycle.

Since the thickness of the Al layer is much larger than its characteristic microstructural dimension, it is suitable to assume that the yield strength of the Al layer is close to that of the bulk material. Using Eqs. (2.10) and (2.12), the theoretical values of ΔT_1 and ΔT_3 are obtained as 33°C and 95°C, respectively, if 35 MPa is used for the yield strength. The results are in good agreement with the experimental observations.

In addition, since the aluminum did not exhibit significant effects of strain hardening and yield strength as a function of temperature in this case, the limiting curvature phenomenon is observed clearly during both the heating and the cooling cycles. Furthermore, by using Eqs. (2.11) and (2.13), the predicted values of κ_e and κ_l are obtained as 0.75 $1/m$ and 1.13 $1/m$, respectively. These values are close to the experimental results, which, for κ_e and κ_l, are 0.7 $1/m$ and 1.5 $1/m$, respectively.

5.1.3 SiO_2-Al Alloy-Si Tri-layer System

This material was processed at MIT Lincoln Laboratory in the same way as the Al alloy-Si bi-layer system. However, the Al-1%Si layer was further passivated with a 1 μm thick SiO_2 coating using plasma-enhanced chemical vapor deposition at 300°C. The system was then subjected to thermal cycling between 20°C and 440°C at a heating and cooling rate step of 10°C/min for three cycles.

The κ-T diagram of the second cycle is shown in Fig. *B-18*. The curvature evolution has not been saturated even after the end of the third cycle. According to [23], more than thirteen cycles may be required to saturate the system due to the complexity of the microstructure.

In Fig. *B-18*, κ varies linearly with T from 20°C to 140°C and then varies nonlinearly with T between 140°C and 220°C. Beyond 220°C, κ not only varies linearly with T again but also reverses its direction until the end of the heating cycle. During cooling, κ varies linearly with T from 440°C to 360°C and then varies nonlinearly with T between 360°C and 180°C. Below 180°C, κ varies linearly with T again but does not reverse its direction (i.e., no curvature reversal phenomenon is observed.) This may be due to the effects of strain hardening and yield strength as a function of temperature.

As discussed in the Al-Si bi-layer system (section 5.1.1), in Fig. *B-18*, the critical temperature change can be obtained as 145°C (T_h) and 110°C (T_c) for the heating and cooling cycles, respectively. Therefore, ΔT_1 (ΔT_3) is 72.5°C and 55°C for the heating and cooling cycles, respectively.

Also, the theoretical values of ΔT_1 and ΔT_3 are obtained by using either Eqs. (2.4) or (2.5) and (2.8), respectively. However, as for the Al-Si bi-layer system, it should be noted that the properties of thin films are very different from the properties of bulk materials. For the 1 μm thick Al film, if the yield strength is 100 MPa, 125 MPa, or 150 MPa, ΔT_1 (ΔT_3) will be 49°C, 62°C, or 74°C, respectively. By comparing the theoretical values with the experimental results, it is reasonable to assume that the Al thin film has a yield strength close to 150 MPa at low temperatures and 125 MPa at

high temperatures. The curvature reversal phenomenon can also be predicted by the previous theoretical work in section 4.1 and Fig. *B-11*. In this system, the thickness ratio of the Si(layer 2)/Al(layer 1) layers is 620, and the ratio is 1 for SiO_2(layer 3)/Al(layer 1) layers; therefore, the system is located at the lower right region of Fig. *B-11*, where systems are expected to experience curvature reversal.

By making a comparison between the results of the Al-Si bi-layer system and the SiO_2-Al-Si tri-layer system, one can find that the results are in reasonable agreement with each other. On the other hand, the difference between the experimental and theoretical results may result from the changes in microstructure and the effects of strain hardening and yield strength as a function of temperature.

5.1.4 SiO_2-Al-Si Tri-layer System

This material was processed at MIT Lincoln Laboratory in a way similar to the SiO_2-Al alloy-Si tri-layer system. Nevertheless, in this system, the passivation layer was 2 μm thick and the metal layer was pure aluminum instead of aluminum alloy. The system was then subjected to thermal cycling between 25°C and 450°C at 10°C/min heating and cooling rate step for three cycles.

Figure *B-19* presents the κ-T diagram of the third cycle and, again, the curvature evolution has not been saturated. In this figure, κ varies linearly with T from 25°C to 120°C and then varies nonlinearly with T between 120°C and 300°C. Beyond 300°C, κ not only varies linearly with T but also reverses its direction until the end of the heating cycle. During cooling, κ varies linearly with T from 450°C to 350°C and then varies nonlinearly with T between 350°C and 180°C. Below 180°C, κ varies linearly with T again and also reverses its direction.

The critical temperature change in this system, as discussed in section 5.1.1, can be obtained as 175°C (T_h) and 130°C (T_c) for the heating and cooling cycles, respectively. Therefore, ΔT_1 (ΔT_3) is 87.5°C and 65°C for the heating and cooling cycles, respectively.

The theoretical values of ΔT_1 and ΔT_3 can be obtained by using either Eqs. (2.4)

or (2.5) and (2.8), respectively. Therefore, if the yield strength of the Al layer is 125 MPa, 150 MPa, or 175 MPa, ΔT_1 (ΔT_3) will be 62°C, 74°C, or 88°C, respectively. By comparing the theoretical and the experimental results, it is reasonable to conclude that the Al thin film has a yield strength of approximately 175 MPa at low temperatures and 125 MPa at high temperatures. In addition, since the ratio of the Si(layer 2)/Al(layer 1) layers thickness is 620 and the ratio of the SiO_2(layer 3)/Al(layer 1) layers is 2, the curvature reversal phenomenon is expected to exist in this system by using either Eq. (4.1) or Fig. *B-11*.

Although there exist some differences between the experimental and theoretical results due to the change of microstructure and the effects of strain hardening and yield strength as a function of temperature, the heating and cooling cycles show nearly perfect symmetry in this system.

5.2 Numerical Check

In this section, numerical analyses are introduced to verify the analytical formulae which are derived in chapters 3 and 4 that determine ΔT_5, curvature reversal, and first yielding interface. MultiTherm [20], a general purpose software developed for numerically estimating the thermomechanical behavior of multi-layered materials, was used. As defined in the previous chapters, layer 1 is the ductile layer and layers 2 and 3 are the brittle layers. All the systems studied in this chapter are assumed to be in an equal biaxial stress state and all material properties are assumed to be independent of temperature. The results show that the analytical predictions are in good agreement with the numerical analyses.

5.2.1 Bi-layer Systems

In this section, the critical temperatures, ΔT_1 and ΔT_5, and the free surface yielding phenomenon are studied in parametric form for two bi-layer systems. In both systems, the yield strength of layer 1 is assumed to be 100 MPa and the mismatch of thermal

expansion coefficients between layers 1 and 2 is $\Delta\alpha = \alpha_1 - \alpha_2 = 20 \cdot 10^{-6}$ $(1/°C)$.

In the first system, the biaxial Young's moduli of the two layers are set to be equal (i.e., $\bar{E}_1 = \bar{E}_2$) and the thickness ratio h_1/h_2 is 2. In the second system, the ratios of the biaxial Young's moduli $\bar{E}_1/\bar{E}_2$ and h_1/h_2 are 10 and 1, respectively. Figures *B-20* to *B-23* show the numerical results of the stress distribution in each layer at several different temperatures.

By examining the ΔT_5 criterion in Fig. *B-9*, it can be seen that the ductile layers in both systems are expected to have free surface yielding before becoming fully plastic. Furthermore, from Fig. *B-9*, ΔT_1 and ΔT_5 are obtained as 90 °C and 155°C, respectively, for the first system and 173 °C and 247°C, respectively, for the second system. Table *A*.1 shows a comparison of the theoretical and numerical results of the two systems.

5.2.2 Tri-layer Systems

In this section, the Si-Al-SiO_2 tri-layer system, is studied for ΔT_1, curvature reversal, and first yielding interface phenomena. As defined in chapter 4, layer 1 is Al, layer 2 is Si, and layer 3 is SiO_2. The properties of each material have already been listed in Tables *A*.8 and *A*.9.

In order to make a systematic comparison, four different geometries are used. The thickness ratios h_2/h_1 are 1, 0.25, 4, and 1 for cases 1, 2, 3, and 4, respectively. The thickness ratios h_3/h_1 of cases 1, 2, 3, and 4 are 4 ,1, 1, and 0.25, respectively. Figures *B-24* to *B-27* show the stress profile in each layer for each case at temperatures near $\Delta T_1 s$. Figures *B-28* to *B-31* display the evolutions of curvatures in each case for the thermal cycling condition $\Delta T = 0°C \rightarrow 150°C \rightarrow 0°C$.

By looking at Fig. *B-11*, the ΔT_1 corresponding to σ_{1y} for each case are 57°C, 70°C, 60°C, and 73°C, respectively. In addition, in Fig. *B-11*, cases 1 and 2 are not expected to have curvature reversal, and consequently, yielding should commence at the interface between layers 1 and 3. Cases 3 and 4 are expected to have curvature reversal, and therefore, plasticity should initiate at the interface between layer 1 and

layer 2. A comparison of the theoretical and the numerical results of the four cases is listed in Table $A.2$.

Chapter 6

Applications

Multi-layered structures are widely used in the design of mechanical, thermal, tribological, electrical, and optical characteristics to extend service lifetime, enhance strength of the surface, or improve performance. Nevertheless, in any type of multi-layered system, thermal residual stresses are induced because of the mismatch of thermal expansion and contraction between different layers during temperature fluctuations. The thermally-induced stresses, if high enough, may cause debonding of the interfaces, cracking and spalling in the ceramic coatings, or yielding and failure in the metallic layers. The current work, on the other hand, provides a general framework to represent the thermal deformation characteristics of multi-layered materials subjected to thermal fluctuations.

In this chapter, a number of typical multi-layered systems which are currently used in engineering applications are listed.

- Table $A.3$: thermal barrier coating systems [24, 25, 28-33];
- Table $A.4$: high temperature corrosion resistant coating systems [24-27, 34-37];
- Table $A.5$: microelectronic systems [25, 38];
- Table $A.6$: magnetic storage devices [26, 39]; and
- Table $A.7$: solid oxide fuel cells [40].

In these tables, the material listed first is the substrate in each system. The properties listed in Tables *A*.8 and *A*.9 [41-48] are for bulk materials at room temperature.

6.1 Thermal Barrier Coatings (TBCs)

Table *A*.3 lists a number of coating systems used as thermal barrier coatings (TBCs), including materials used and processing method adopted. Thermal barrier coatings are widely used in the engine industry for metallic components such as aircraft gas turbines, airfoils, high temperature combustors, liners, turbine gas path surfaces, and turbine nozzles which experience high temperature (1000°C or higher) effects. A TBC system is usually composed of a metallic bond coat, which has a thickness about hundreds of micrometers, applied to the metal component, followed by a ceramic layer (topcoat), several hundred micrometers in thickness. The most commonly selected ceramics are magnesium oxide- (MgO), calcium oxide- (CaO), cerium oxide- (CeO_2), and yttria-stablized zirconia. Zirconia's low thermal conductivity can reduce the temperature within the metal substrate dramatically and its high thermal expansion coefficient can reduce the stresses within both the coating and the substrate due to temperature change. The metallic bond coat usually is MCrAlY (M=Ni, Co, or Fe). For TBC systems operating under an high temperature environment, the substrate typically is a Ni-based or Co-based superalloy such as Mar-M-200+hf or Mar-M-509.

Although TBC systems can prevent spallation that results from the thermal shock from rapid heating and cooling that is experienced in gas turbines or diesel engines, due to the mismatch of thermal expansion coefficients between metals and ceramics, thermal stresses are inevitably induced during temperature fluctuations. By applying the formulae provided in chapters 2 to 4, it can be found that despite the induced thermal stress in the substrate (i.e., the metal layer) is low, however, due to the effect of geometry (thin coatings and thick substrates), the stress is very high in the coatings. Therefore, how to lower the high thermal stress in ceramics to avoid failure is a matter of deep concern in TBC systems Furthermore, by examining Fig. *B-9*, one can find that most of these systems are located in the right portion of the figure. This

indicates that, under certain conditions, free surface yielding may happen in metal layers before they become fully plastic. This phenomenon becomes important when systems subjected to cyclic deformation. In fatigue, cracks usually initiate at the free surface if there is accumulated plastic strain.

6.2 High Temperature Corrosion Resistant Coatings

Table *A*.4 lists several systems which are applied as high temperature corrosion resistant coating systems, including materials used and processing methods adopted. Oxidation and corrosion are major concerns for materials exposed to high temperatures and aggressive gaseous environments containing sulphur, oxygen, or both, such as in aero gas turbines, nuclear process heat plants, coal gasification plants. Coatings for this application are aimed to protect alloys (substrate) from rapid oxidation and embrittlement at elevated temperatures. Although metallic coatings are the most common choice for moderate working temperatures, refractory oxides or ceramics are better material choices to provide protection from oxidation and corrosion under high temperature detrimental operating environments.

On the other hand, due to the mismatch of thermal expansion coefficients between metals and ceramics, thermal stresses are induced by temperature fluctuations. Like discussed in the TBC systems, by applying the formulae derived in chapters 2 to 4, one can find that the induced thermal stress in the metal layer is low and the stress is very high in the coatings. By looking at Fig. *B-9*, it can be found that most of these systems are also located in the right portion of the figure. Therefore, how to lower the high thermal stress in ceramics and, to avoid free surface yielding are important in these systems.

6.3 Electronic Materials

Table *A*.5 lists several electronic thin film systems. They can be divided into three categories:

- interconnecting structure in integrated circuits,
- semiconductors, and
- multi-chip modules for electronic packaging.

In contrast to thermal barrier coating and high temperature oxidation/corrosion resistant coating systems where the substrates are metals, most substrates in microelectronic systems are ceramics such as silicon, sapphire, aluminum oxide (Al_2O_3), beryllia (BeO), and aluminum nitride (AlN). The substrate thickness is about hundreds of micrometers and the thin film thickness and the passivation layer thickness are several micrometers.

By going through the same procedures discussed in chapter 3 and chapter 4, a similar engineering diagram can be easily constructed. For instance, if the system, Si-Al-SiO_2, is selected (i.e., Fig. *B-11* will be constructed), one can find that ΔT_1 and ΔT_3 are very low. In other words, the metal layer easily yields. Therefore, how to avoid plastic deformation in metal layers is crucial in the design of microelectronic systems. Moreover, Fig. *B-11* shows that this system is likely to have curvature reversal. This is because that the thickness ratio of the passivation and the metal layers is close to 1, and the ratio of the substrate and metal layer is close to 100. The curvature reversal phenomenon provides another degree of freedom in the design of microelectronic systems.

6.4 Magnetic Storage Devices

Table *A*.6 lists some typical materials used in magnetic storage devices. For recording tapes and floppy disks, a polyethylene terepthalate (PET) substrate usually is coated with magnetic particles, such as CrO_2, γ-Fe_2O_3, and a polymetric binder such as

polyester-polyurethane, polyether-polyurethane, nitrocellulose, poly(vinyl chloride), poly(vinyl alcohol-vinyl acetate), poly(vinylidene chloride), phenoxy, or epoxy. On tapes, a substrate generally has a thickness of 12 to 36 μm and is coated with a 2 to 5 μm thick magnetic coating. The substrate on floppy disks is thicker (75 μm) and is coated on both sides. The substrate for rigid disks is usually a 1.3 to 1.9 mm thick non-heat-treatable Al-Mg alloy 5086. For particulate disks, the substrate is covered with a chromate conversion coating (<100 nm), and then spin-coated with a 1 to 2 μm thick magnetic coating. For thin film disks, the same substrate is plated either with a 10 to 20 μm thick electroless Ni-P layer or a 2 to 20 μm thick alumite layer. The substrate is then coated with a magnetic film and may be passivated with a 20 to 30 nm thick protective overcoat such as sputtered or spin-coated SiO_2, sputtered yttria-stablized zirconia, plated rhodium and chromium, or sputtered diamond-like carbon. The magnetic coating is typically 25 to 150 nm thick and composed of γ-Fe_2O_3 and a hard copolymer (of phenolic, polyurethane, or epoxy) binder. A newly developed system is listed in the bottom of Table *A*.6. This system uses chemically strengthened glass as a substrate that is sputter-coated with a 200 nm thick chromium film. The magnetic medium, made of a cobalt-based alloy, is sputtered onto the chromium film to a thickness of 80 nm. Finally, a 40 to 45 nm carbon overcoat is sputtered on the top of the magnetic medium.

Due to the effect of geometry, by looking at Fig. *B-9*, one can find that most of the magnetic storage device systems are located in the right portions of Fig. *B-9* (i.e., ΔT_1 and ΔT_3 are high). Moreover, by using the formulae derived in chapters 2 to 4, one can find that the stress in the substrates is low and the stress in the coatings is high. Since temperature fluctuation is not strong in these systems, the free surface yielding is not expected to happen. Nevertheless, since the processing temperature for those systems is sometimes as high as several hundred degrees centigrade, it is still necessary to pay attention to the intrinsic stress in the coatings due to the processing.

6.5 Solid Oxide Fuel Cells (SOFCs)

Solid oxide fuel cells (SOFCs) are another area of application that concerns about the stresses induced during high working temperatures. SOFCs have received a lot of attention in the power generation industry because of advantages such as high energy conversion efficiency and low production of pollutants. A SOFC is an energy conversion device that produces electricity by chemical reaction of a fuel (e.g. hydrogen) and an oxidant (e.g. oxygen). A SOFC element is composed of four parts: interconnect, anode, electrolyte, and cathode. The most common materials used in each part are doped lanthanum chromite ($LaCrO_3$) for interconnect, nickel/yttria stabilized zirconia cermet for anode, doped lanthanum manganite ($LaMnO_3$) for cathode, and yttria (Y_2O_3)-fully stabilized ZrO_2 for electrolyte.

Due to the fact that a lot of heat is dissipated while generating electricity, the temperature near the cell maybe as high as 1000°C. The combination of this high temperature and the mismatch of thermal expansion coefficients between parts creates stresses inside the cell. If the stresses are high enough, the cell will fail. Therefore, it becomes important to look at the thermally induced stresses. Although practical cells are operated as a stack (i.e., elements are connected in electrical series), the formulations that have been discussed still can be applied to a single element to provide general features. Table *A*.7 lists a number of common materials (some with thermal expansion coefficients listed) used in each part of a SOFC element.

Chapter 7

Conclusions and Future Work

In this chapter, a number of conclusions are made regarding the analytical formulations and special phenomena obtained in the current study. Based on these results, several possible future work is suggested in this chapter.

7.1 Conclusions

In the present work, a number of analytical formulations and specific cases of elasto-plastic deformation in multi-layered materials are derived and examined. General engineering diagrams for elastic and plastic deformation of multi-layered materials are also constructed. Those results are compared with experimental and numerical results. In this section, a number of important conclusions are listed:

- The general framework for the representation of the thermoelastic and thermo-plastic deformation characteristics of multi-layered materials with applications in structural components, microelectronics, magnetic systems, and solid oxide fuel cells is presented,

- The closed-form solution for theoretical maximum normalized elastic curvature for an arbitrary bi-layer composite is derived, and the value of the maximum normalized elastic curvature is obtained as 1.5, which occurs at $h_1/h_2 = (E_2/E_1)^{1/2}$,

- The closed-form solution for the conditions governing the temperature, ΔT_5, at which the onset of yielding at the free surface of a general bi-layer composite occurs, is derived,

- The critical criteria for the occurrence of curvature reversal and the prediction of the interface at which yielding initiates for a general tri-layer material are obtained separately, and these two criteria are the same,

- The effects of Young's modulus, specimen geometry, the thermal expansion coefficient, and yield strength on the overall elasto-plastic response of multi-layered materials are investigated,

- ΔT_1 and ΔT_3 are almost equal when a ductile layer has a much smaller thickness (i.e., the bi-layer system is a thin ductile film on a thick brittle substrate) and Young's modulus than the substrate does,

- The free surface yielding phenomenon, for bi-layer systems, occurs only if the thickness and/or the Young's modulus of a ductile layer are large enough compared to those of a brittle layer,

- The analytical results are in reasonable agreement with experimental results although there are some discrepancies due to the complexity of microstructure and texture and the effects of strain hardening and yield strength as a function of temperature,

- Engineering diagrams for elastic and plastic deformation of general multi-layered materials are constructed in a parametric form, and

- Materials and their properties for a number of typical multi-layered systems which are used in applications such as thermal barrier coatings, oxidation/corrosion resistant coatings, magnetic storage devices, solid oxide fuel cells, and electronic systems, are collected and analyzed.

7.2 Future Work

Based on the conclusions obtained in the current work, a number of research directions for future work are suggested:

- Detailed examination of the microstructure evolution and the interdiffusion phenomenon are required to explain the discrepancies between the analytical and experimental results,
- To obtain a linkage between the microscopic behavior, such as texture evolution, and the macroscopic behavior, such as curvature evolution, through the study of microstructure, and
- Extensive work on multi-layered materials with many alternating layers of ductile and brittle materials could follow the basic outline of the present work. It can be shown that plasticity will commence at one of the interfaces, possibly the one closest to the stiffer brittle layer and away from the free surface [13].

Appendix A

TABLES

Table A.1: Theoretical and Numerical Results for Two-Layer Systems

	System 1	System 2
$\bar{E}_1/\bar{E}_2$	1	10
h_1/h_2	2	1
σ_{1y}(MPa)	100	100
$\Delta\alpha \cdot 10^{-6}(1/°C)$	20	20
theoretical $\Delta T_1(°C)$	90	175
numerical $\Delta T_1(°C)$	91	175
theoretical $\Delta T_5(°C)$	155	247
numerical $\Delta T_5(°C)$	155	248

Table A.2: Theoretical and Numerical Results for Three-Layer Systems

	Case 1	Case 2	Case 3	Case 4
h_2/h_1	1	0.25	4	1
h_3/h_1	4	1	1	0.25
theoretical $\Delta T_1(°C)$	57	70	60	73
numerical $\Delta T_1(°C)$	57	70	58	74
first yielding interface (predicted)	1/3	1/3	1/2	1/2
first yielding interface (simulated)	1/3	1/3	1/2	1/2
curvature reversal (predicted)	no	no	yes	yes
curvature reversal (simulated)	no	no	yes	yes

Table A.3: Thermal Barrier Coatings

Material	processing
Steel /MCrAlY/ ZrO_2	Plasma spraying
Mar-M-509/MCrAlY/ZrO_2	Plasma spraying
Steel/Al_2O_3	Reactive sputtering
Ni alloy/Si_3N_4	CVD
Steel/$MoSi_2$	CVD
W/ZrO_2	Plasma spraying
W/SiC	CVD
W/ThO_2	-

Table A.4: High Temperature Corrosion Resistant Coatings

Material	processing
Ni-based alloy/Si_3N_4	CVD
Co-based alloy/Si_3N_4	CVD
Mo/$MoSi_2$	Vacuum plasma spraying
Mo/SiO_2	CVD
Mo/Al_2O_3	thermal spray
Mo/ZrO_2	thermal spray
Nb/$MoSi_2$	Vacuum plasma spraying
Steel/SiO_2	CVD
Steel/CeO_2	-
Steel/Al_2O_3	Reactive sputtering
Steel/Cr_2O_3	Plasma spraying
Steel/ZrO_2	Plasma spraying
Mar-M-509/MCrAlY/ZrO_2	Plasma spraying

Table A.5: Electronic Coating Systems

Interconnecting Structure in Integrated Circuits		
Si/Al	Si/Au	Si/Ag
$Si/Al/SiO_2$	$Si/Cu/SiO_2$	$Si/Cu/Si_3N_4$
Quartz/Polyimide/Cu	Quartz/Polyimide/Cr	Si/PSG
Multi-Chip Module for Electronic Packaging		
BeO/Cu	BeO/Al	Al_2O_3/Cu
$Si/Cu/SiO_2$	$Al_2O_3/Al/SiO_2$	AlN/Cu/Polyimide
Semiconductors and Opto-Electronic Applications		
Si/GaAs	Si/SiGe	Si/InSb
GaAs/ZnSe	GaAs/CdTe	GaAs/InP
Sapphire/Si	Sapphire/GaN	GaAs/InGaAs
$GaAs/Si/Si_3N_4$	GaAs/Ge/TiN	

Table A.6: Magnetic Recording Devices

Material	Thickness	Application
polyethylene terepthalate (PET) magnetic coating back coating(optional)	12-36um 2-5um 2-5um	Tape
polyethylene terepthalate (PET) magnetic coating magnetic coating(back coating)	75um 2-5um 2-5um	Floppy-disk
Al-Mg(substrate) chromate conversion coating magnetic coating	1.3-1.9mm <100nm 1-2um	Rigid disk (particulate)
Al-Mg(substrate) electroless (90wt%Ni-10wt%P) magnetic coating protective overcoating	1.3-1.9mm 10-20um 25-150nm 20-30nm	Rigid disk (thin-film) with metallic magnetic layer
Al-Mg(substrate) alumite magnetic coating protective overcoating	1.3-1.9mm 2-20um 25-150nm 20-30nm	Rigid disk (thin-film) with oxide magnetic layer
glass substrate chromium Co-alloy medium carbon	1.9mm 200nm 80nm 40-45nm	Rigid disk (thin-film) glass-based substrate

Table A.7: Solid Oxide Fuel Cells

Part	Material	$\alpha \cdot 10^{-6}(1/°C)$
interconnect	doped lanthanum chromite ($LaCrO_3$)	6.7
	yttrium chromite ($YCrO_3$)	-
anode	nickel(30vol%)/YSZ	12
	cobalt/YSZ	-
electrolyte	yttria (Y_2O_3)fully stabilized ZrO_2	10
	ceria (CeO_2) doped with CaO or Y_2O_3	10
	stabilized bismuth oxide (Bi_2O_3)	-
cathode	doped lanthanum manganite ($LaMnO_3$)	12
	doped lanthanum cobaltite ($LaCoO_3$)	23

Table A.8: Material Properties for Selected Ceramics

Material	$E(GPa)$	ν	$\alpha{\cdot}10^{-6}(1/^{\circ}K)$	σ_y(MPa)
Si_3N_4	300	0.22	2.3	-
Al_2O_3	372	0.25	7	-
ZrO_2	200	0.26	10	-
$MoSi_2$	344	0.17	8.1	-
SiC	380	0.19	4.3	-
ThO_2	234	0.29	9.5	-
Cr_2O_3	105	0.2	7.5	-
SiO_2	80	0.18	1	-
BeO	380	0.34	7.4	-
AlN	339	0.24	5.5	-
TiN	320	0.19	8.1	-
Quartz	73	0.17	0.5	-
PSG	90	0.25	1.8	-
$In-0.12Ga_{0.88}As$	81	0.3	8	-
GaAs(100)	86	0.31	6.9	-
Ge(100)	103	0.27	5.8	-
Si(100)	130	0.28	3	-
Polyimide	3	0.36	40	-

Table A.9: Material Properties for Selected Metals

Material	$E(GPa)$	ν	$\alpha \cdot 10^{-6}(1/^{\circ}K)$	σ_y(MPa)
Tool Steel	210	0.3	10	1000-1400
Stainless Steel	210	0.3	14	200-2000
Carbon Steel	210	0.3	14	200-600
Ni-based alloy	200	0.3	12	180-1000
Co-based alloy	240	0.3	14	500-700
W	345	0.3	4.6	150
Mo	324	0.31	4.9	300
Nb	100	0.38	7.9	150
Al	62	0.33	25	35
Cu	125	0.34	16.5	60
Au	70	0.42	16.5	30
Ag	83	0.36	19	54

Appendix B

Figures

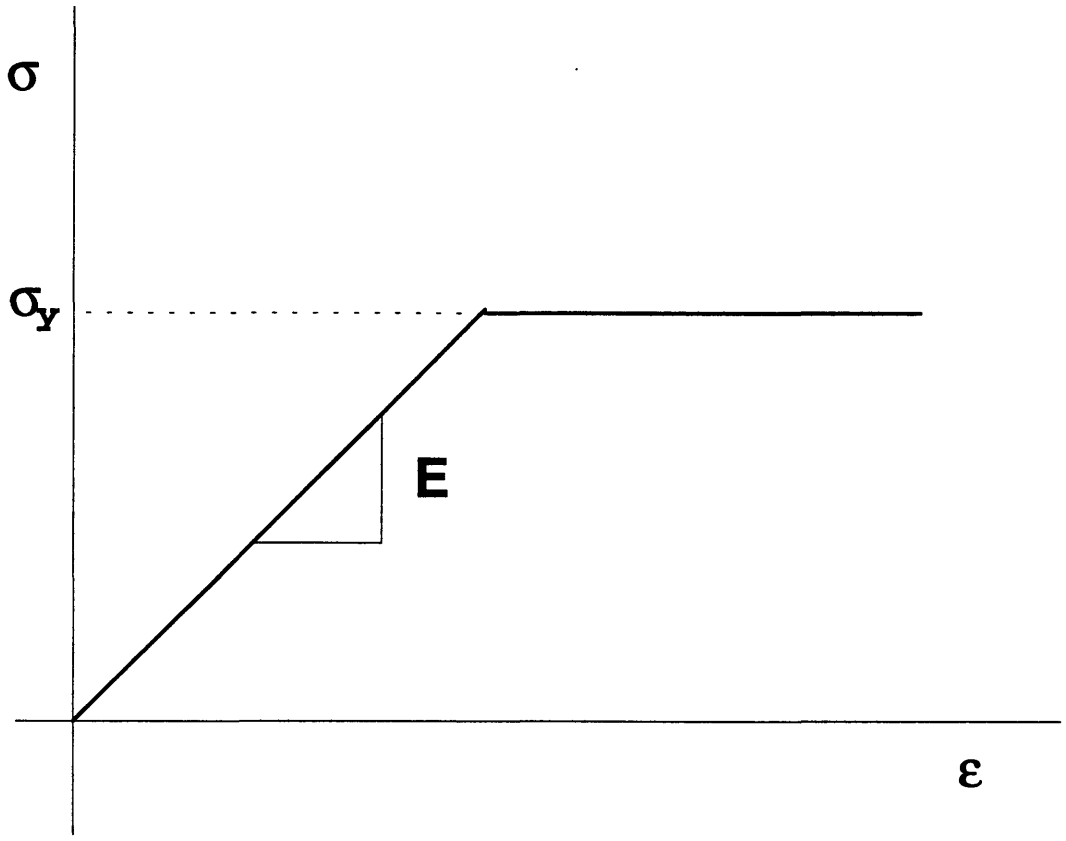

Figure B-1: The stress-strain response of a ductile layer.

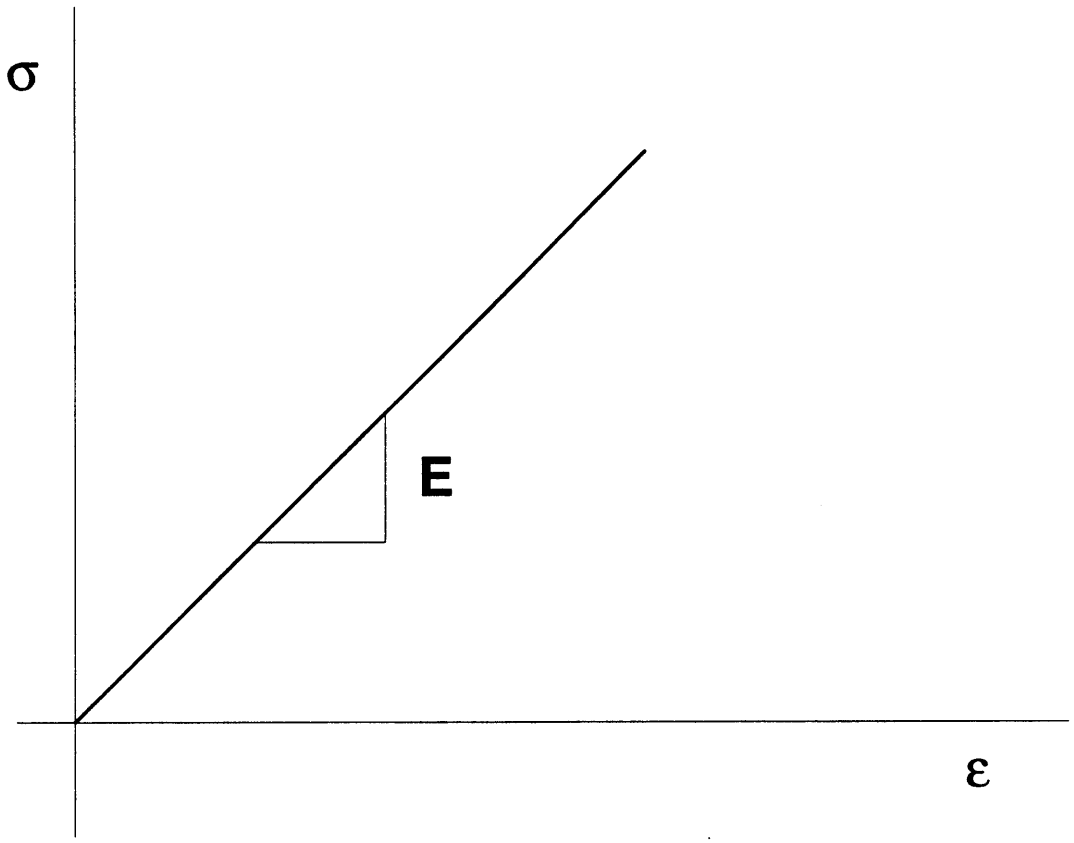

Figure B-2: The stress-strain response of a brittle layer.

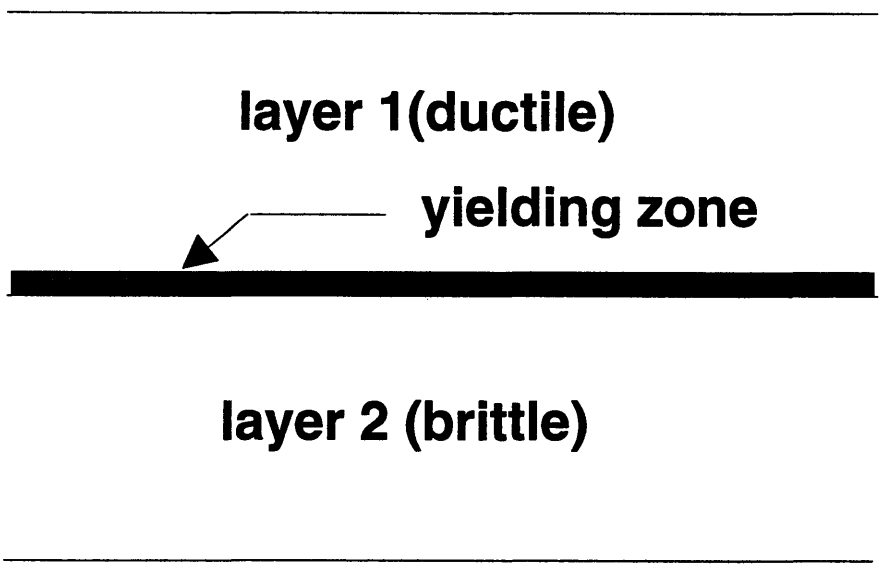

Figure B-3: The schematic diagram of the initiation of yielding of layer 1 at $\Delta T = \Delta T_1$.

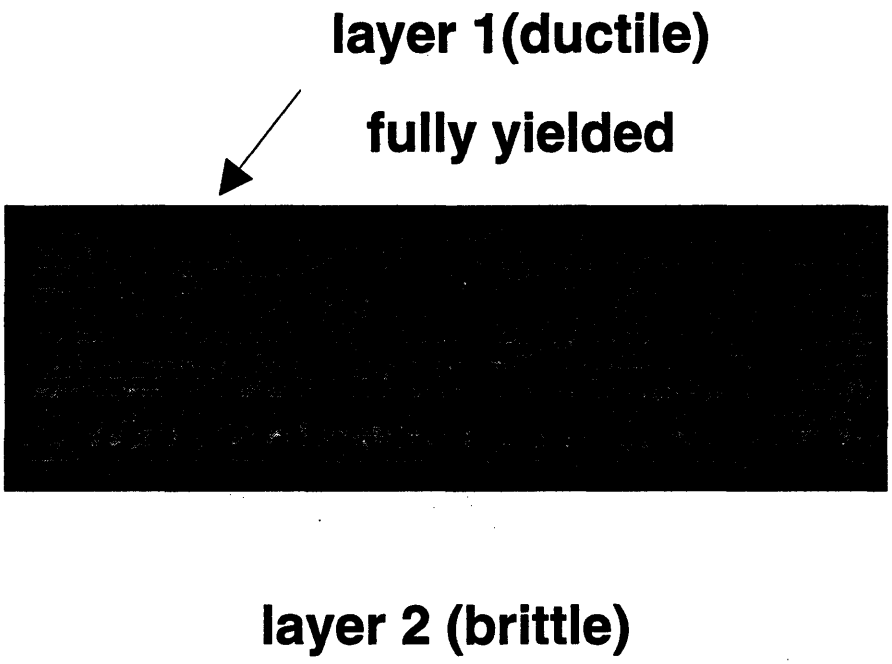

Figure B-4: The schematic diagram of full yielding of layer 1 at $\Delta T = \Delta T_3$.

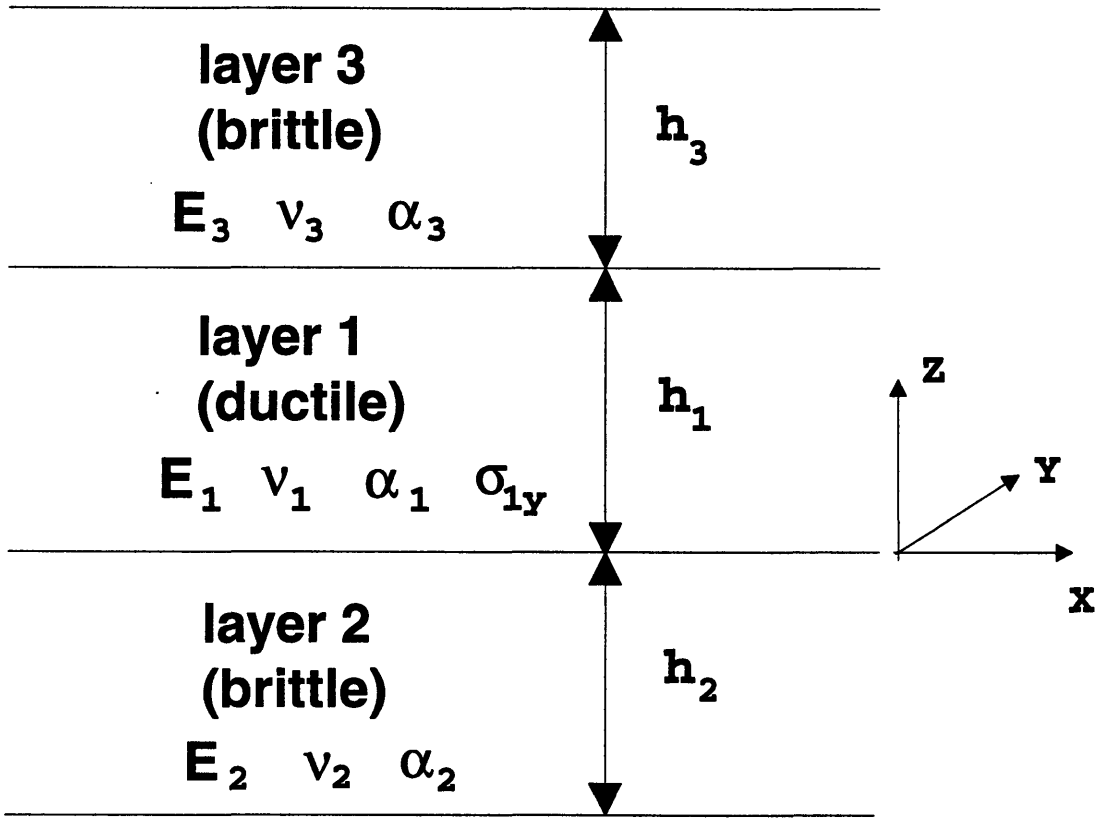

Figure B-5: The schematic in-plane geometry of a tri-layer material.

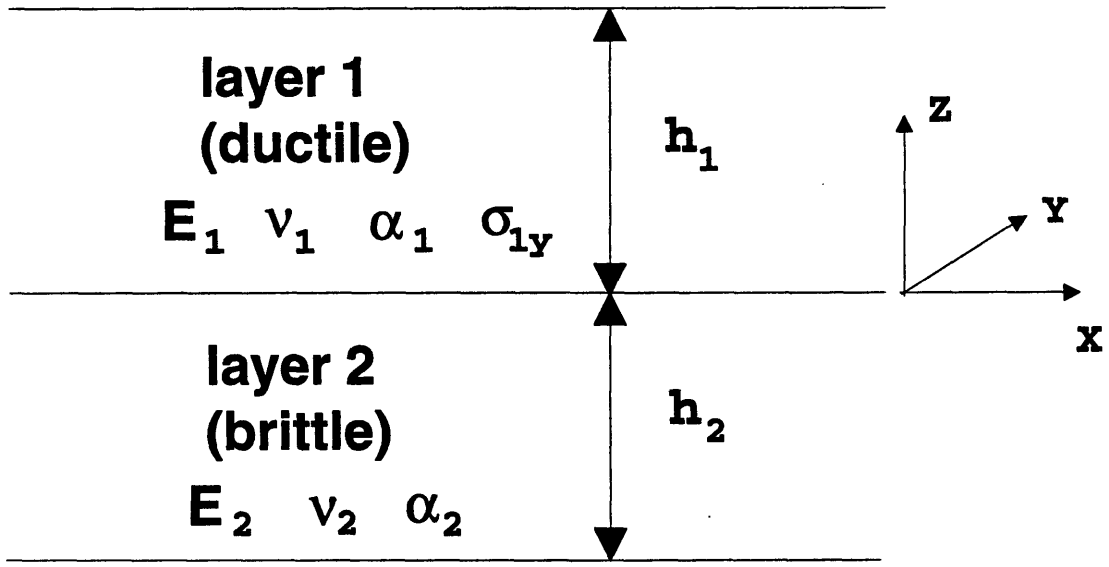

Figure B-6: The schematic in-plane geometry of a bi-layer material.

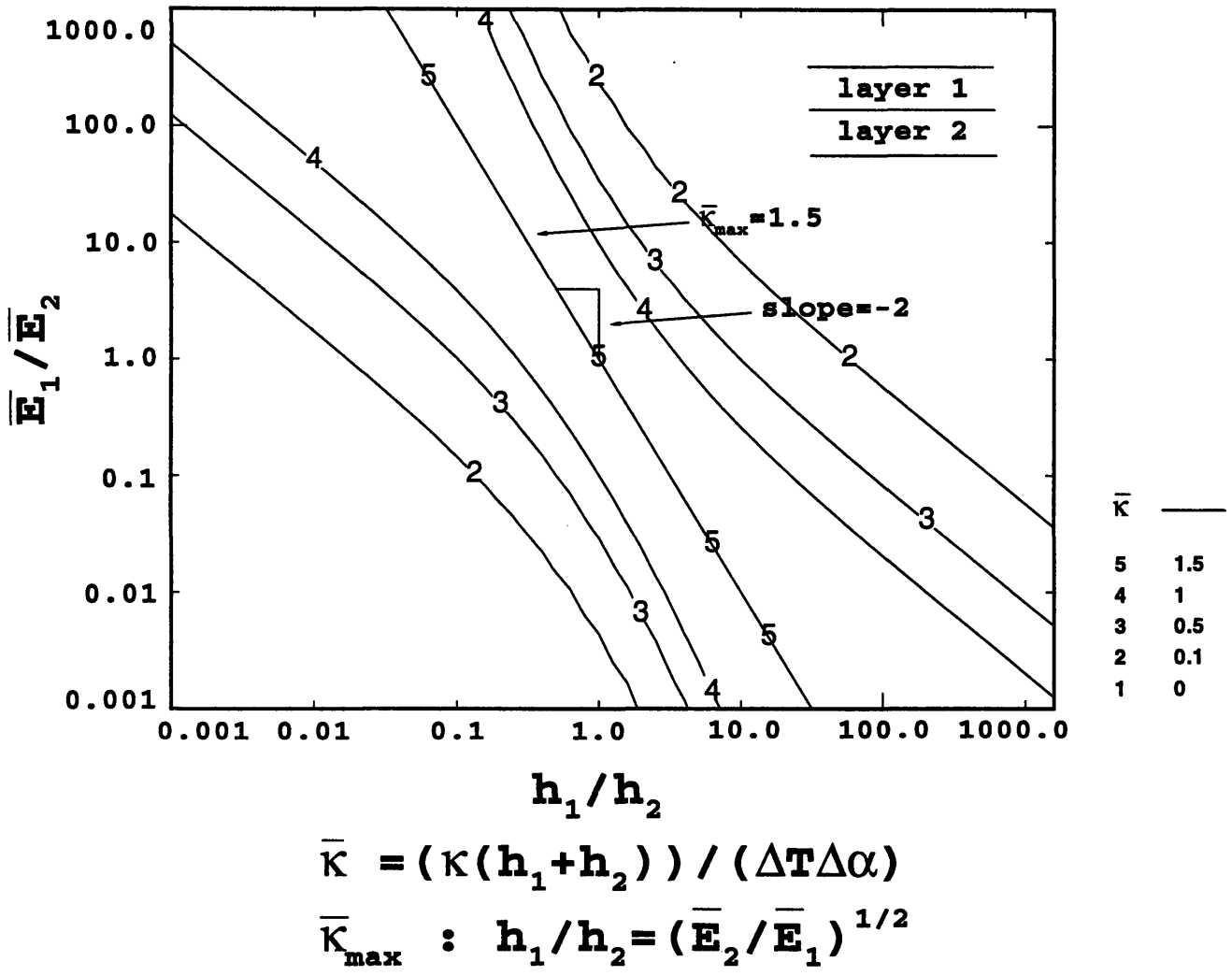

Figure B-7: The normalized elastic curvature with $\bar{E}_1/\bar{E}_2$ and h_1/h_2 for bi-layer systems.

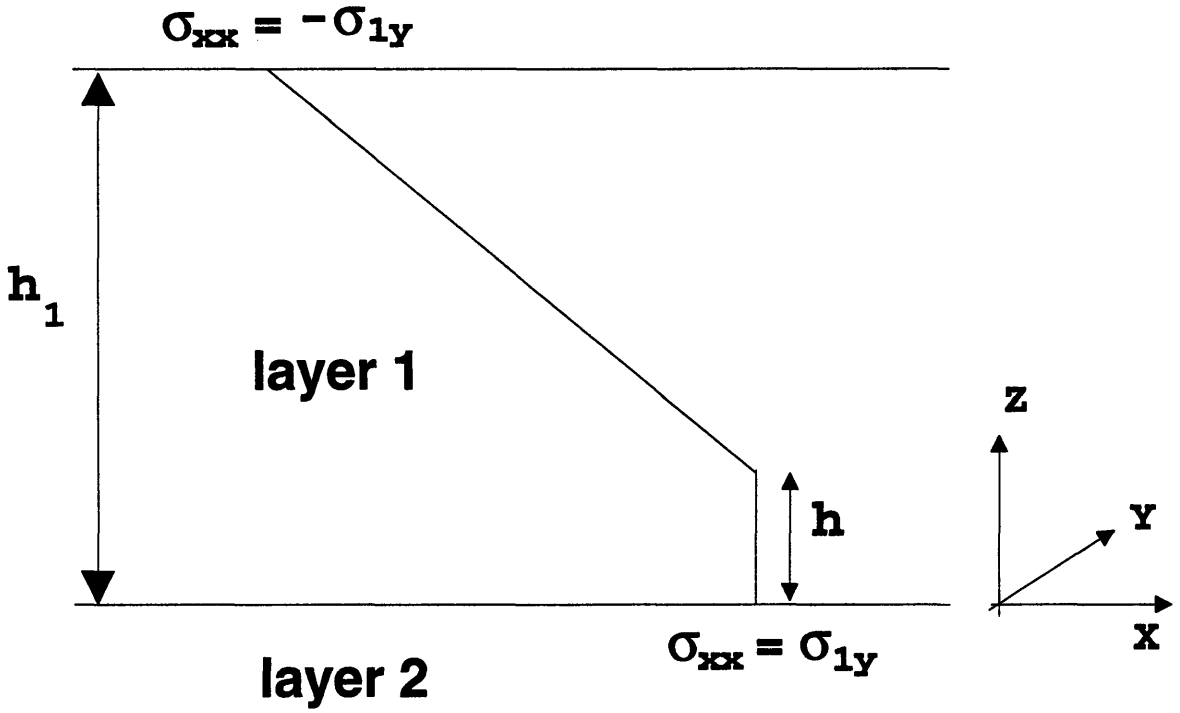

Figure B-8: Schematic profile of stress distribution in a ductile layer at ΔT_5 for bi-layer systems.

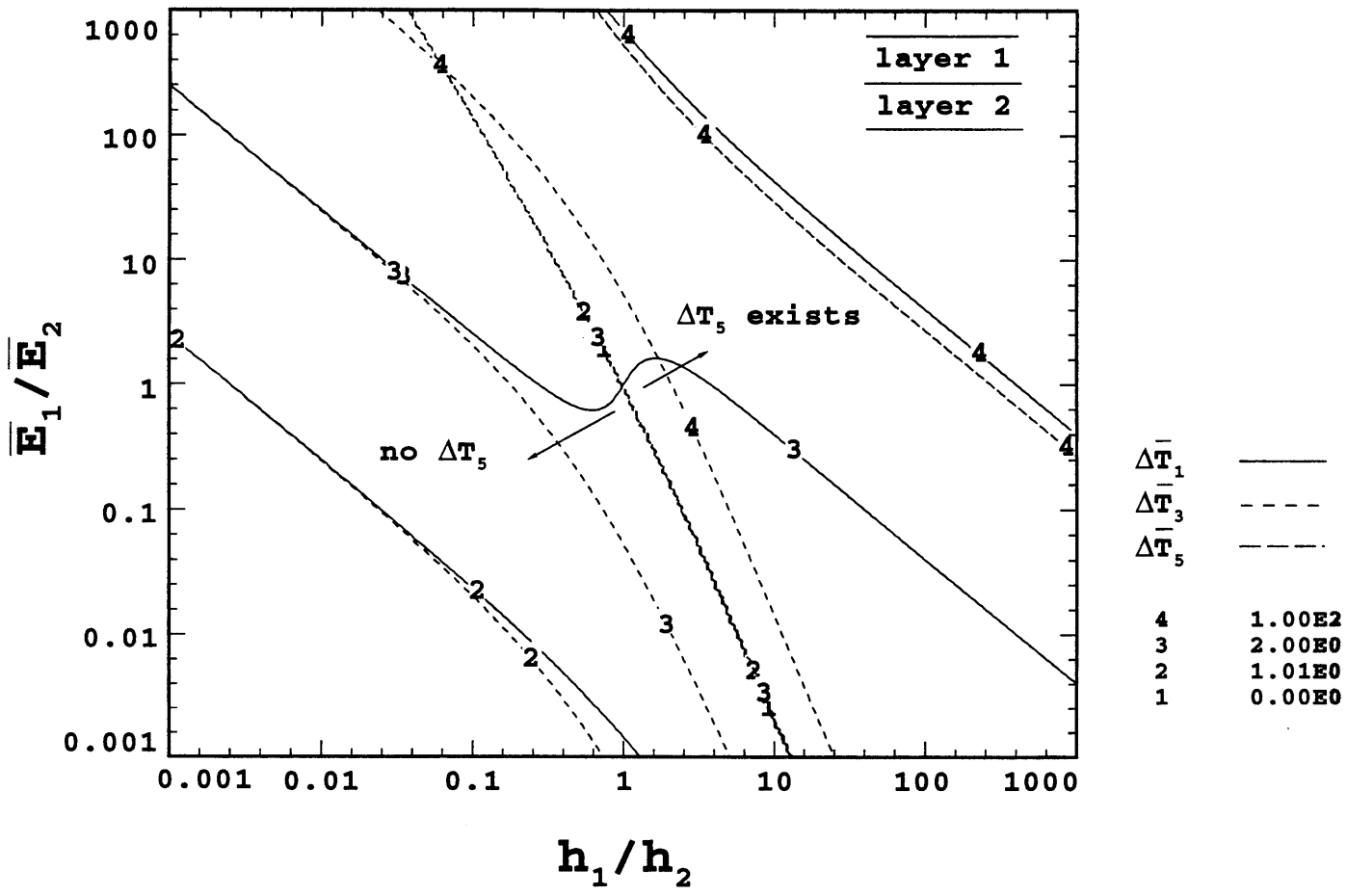

Figure B-9: The characteristic temperatures ΔT_1, ΔT_3, and ΔT_5 with $\bar{E}_1/\bar{E}_2$ and h_1/h_2 for bi-layer systems.

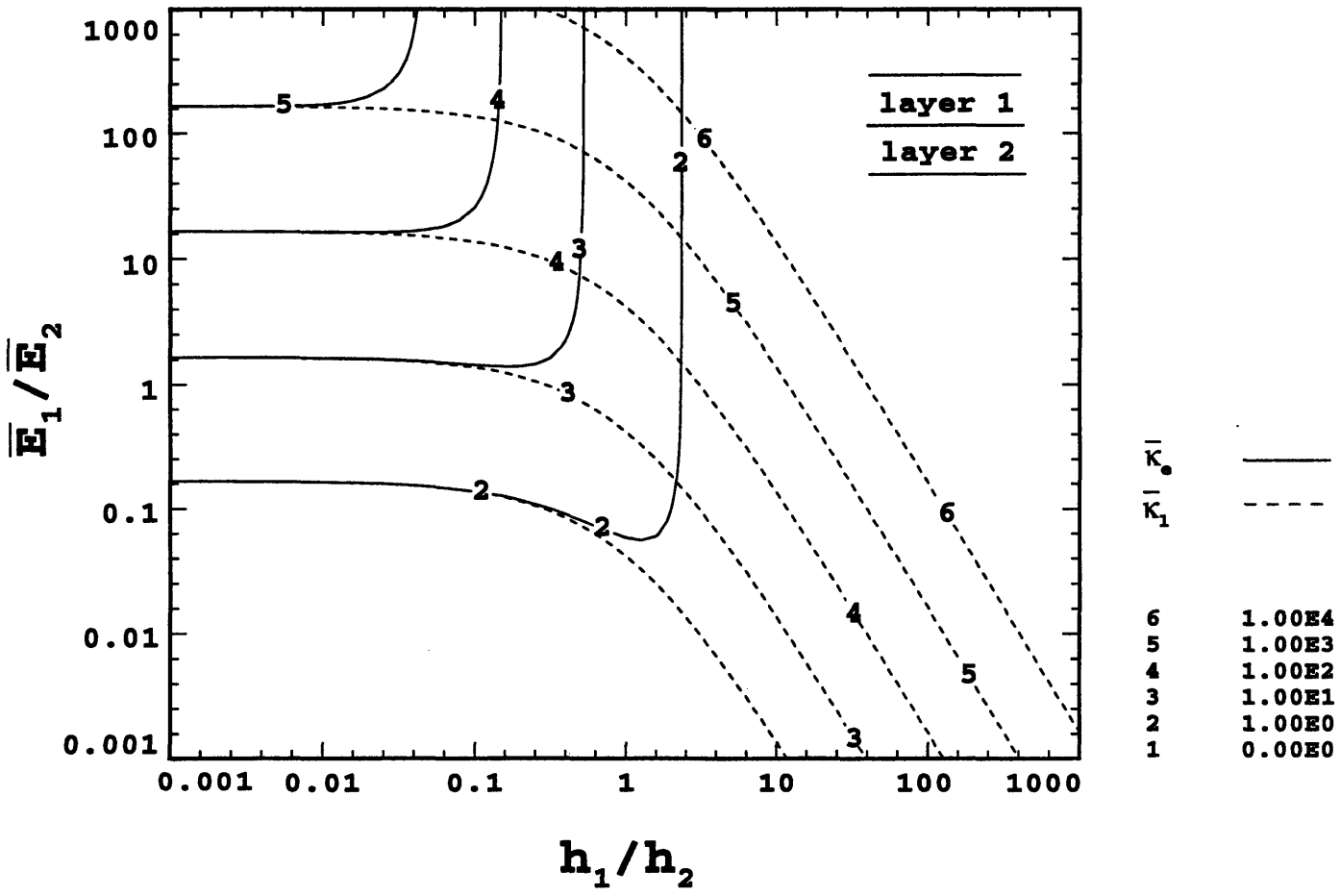

Figure B-10: The evolution of normalized elastic and plastic limiting curvatures $\bar{\kappa}_e$ and $\bar{\kappa}_l$ with $\bar{E}_1/\bar{E}_2$ and h_1/h_2 for bi-layer systems.

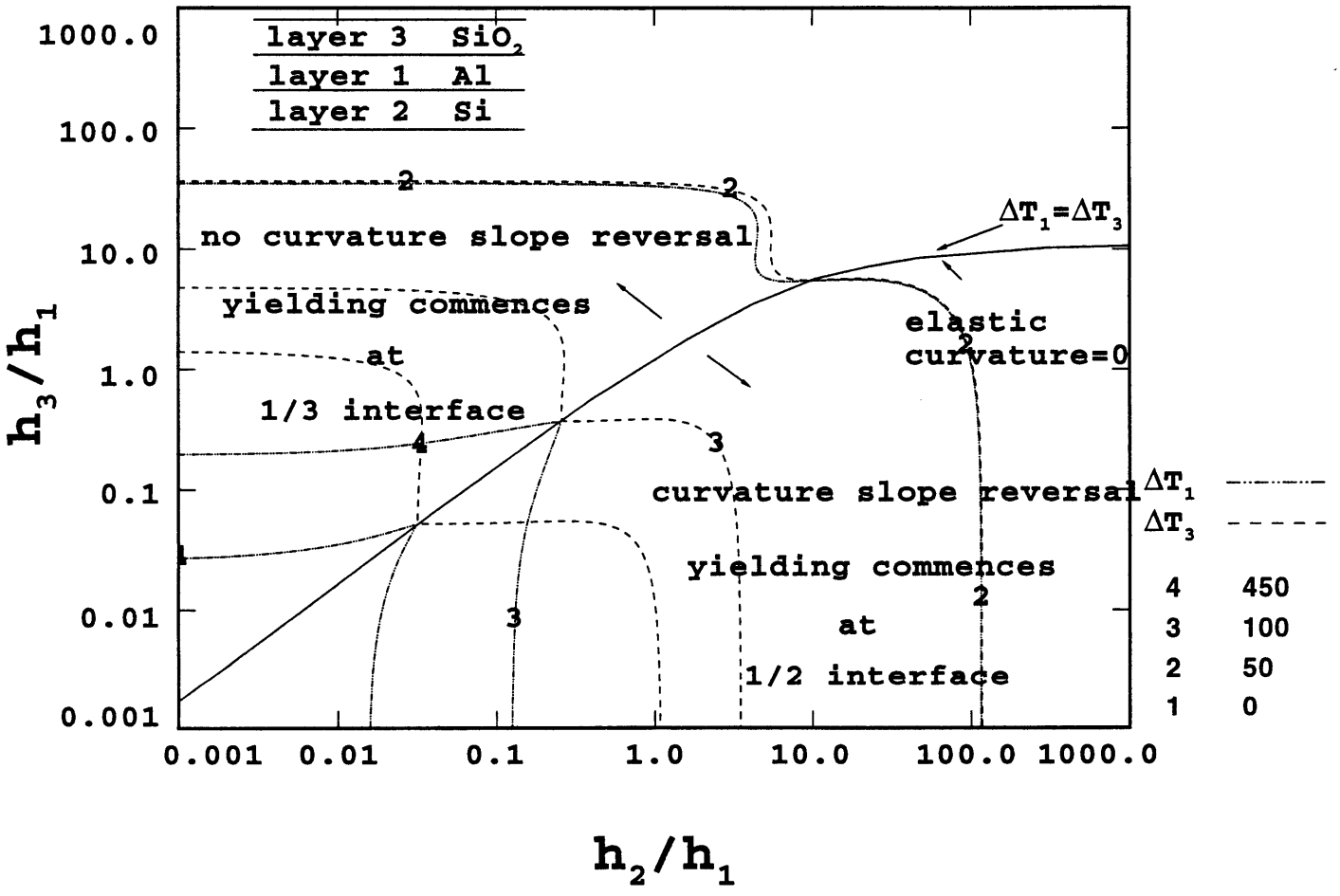

Figure B-11: The characteristic temperatures ΔT_1 and ΔT_3 with h_2/h_1 as well as h_3/h_1 for the specific system Si-Al-SiO_2.

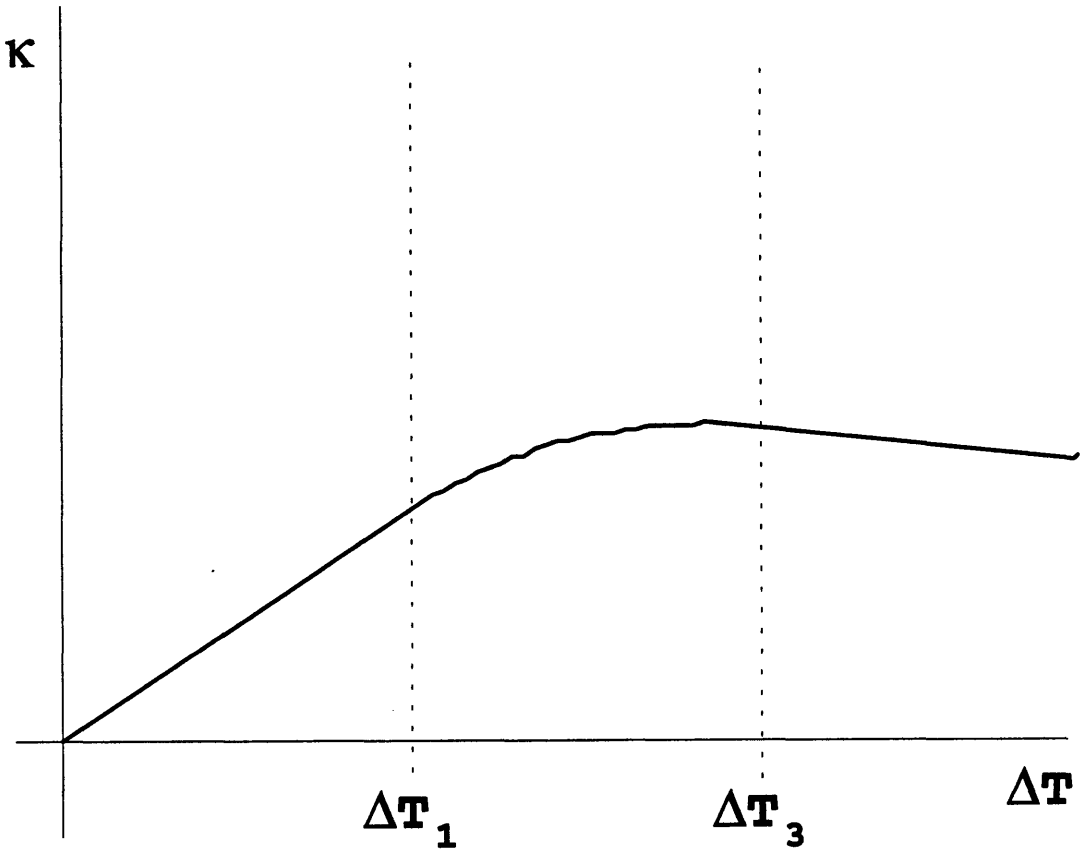

Figure B-12: One type of κ-T schematic diagram with curvature reversal.

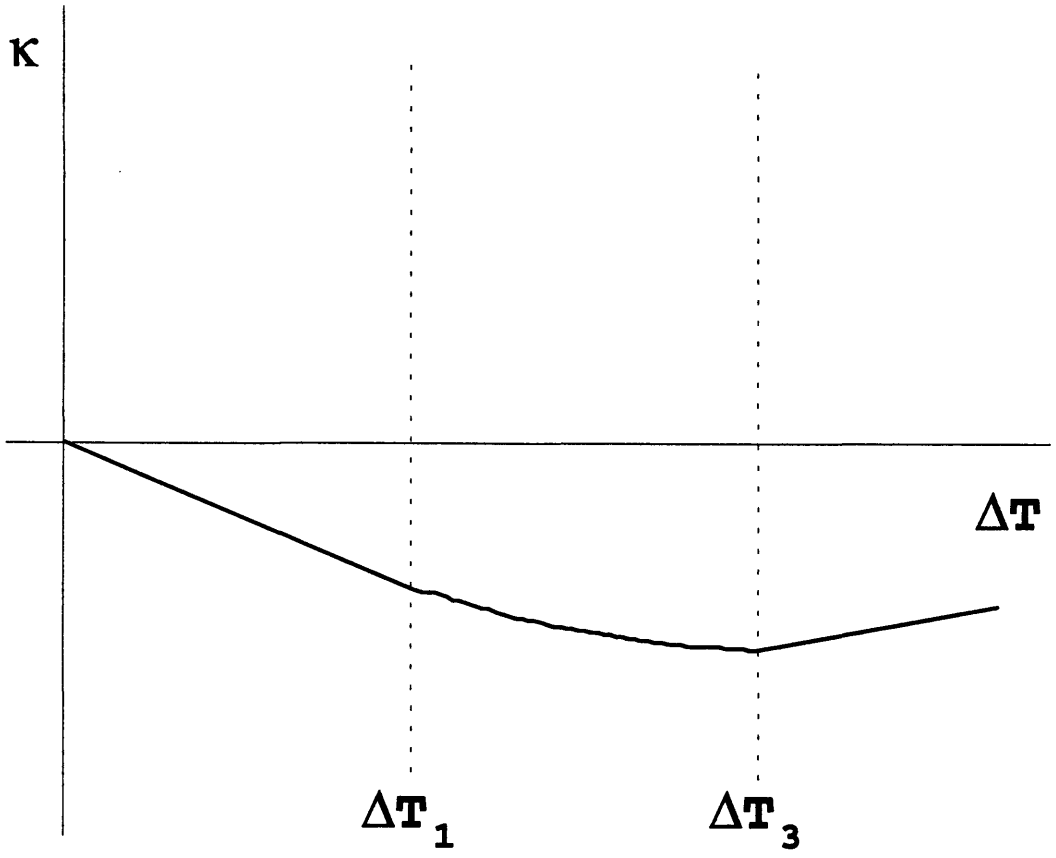

Figure B-13: Another type of κ-T schematic diagram with curvature reversal.

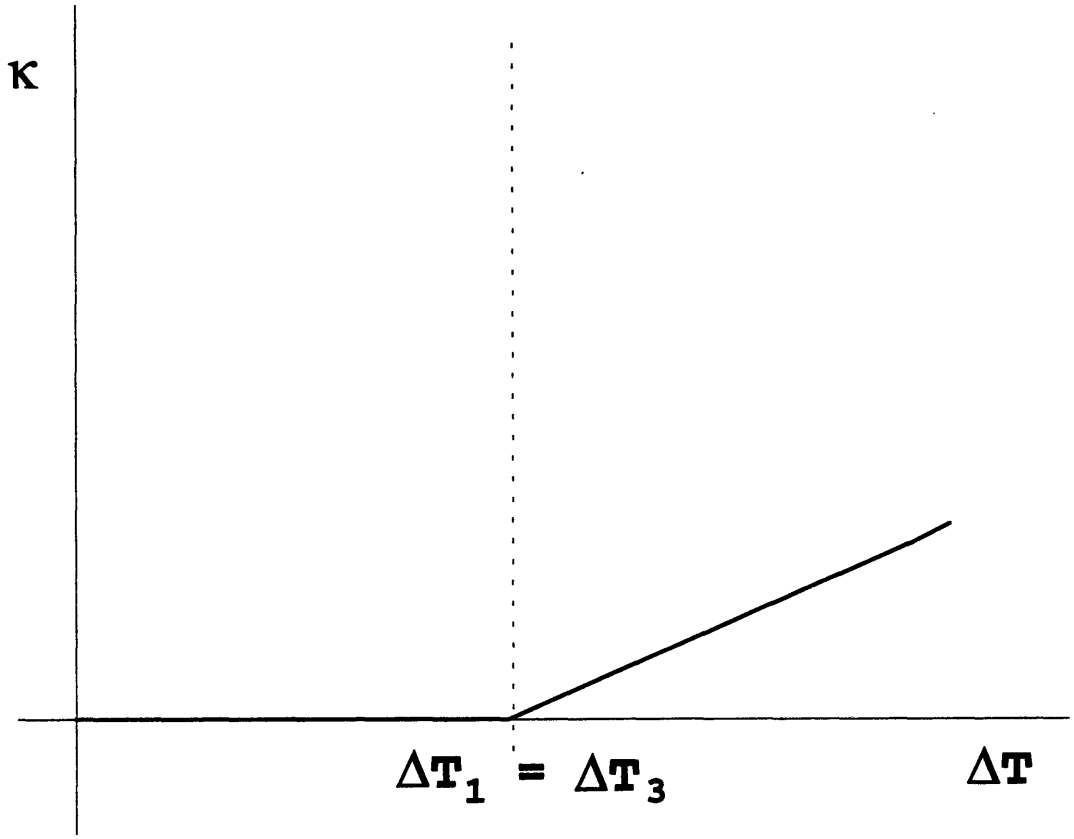

Figure B-14: One type of κ-T schematic diagram with curvature reversal (critical condition).

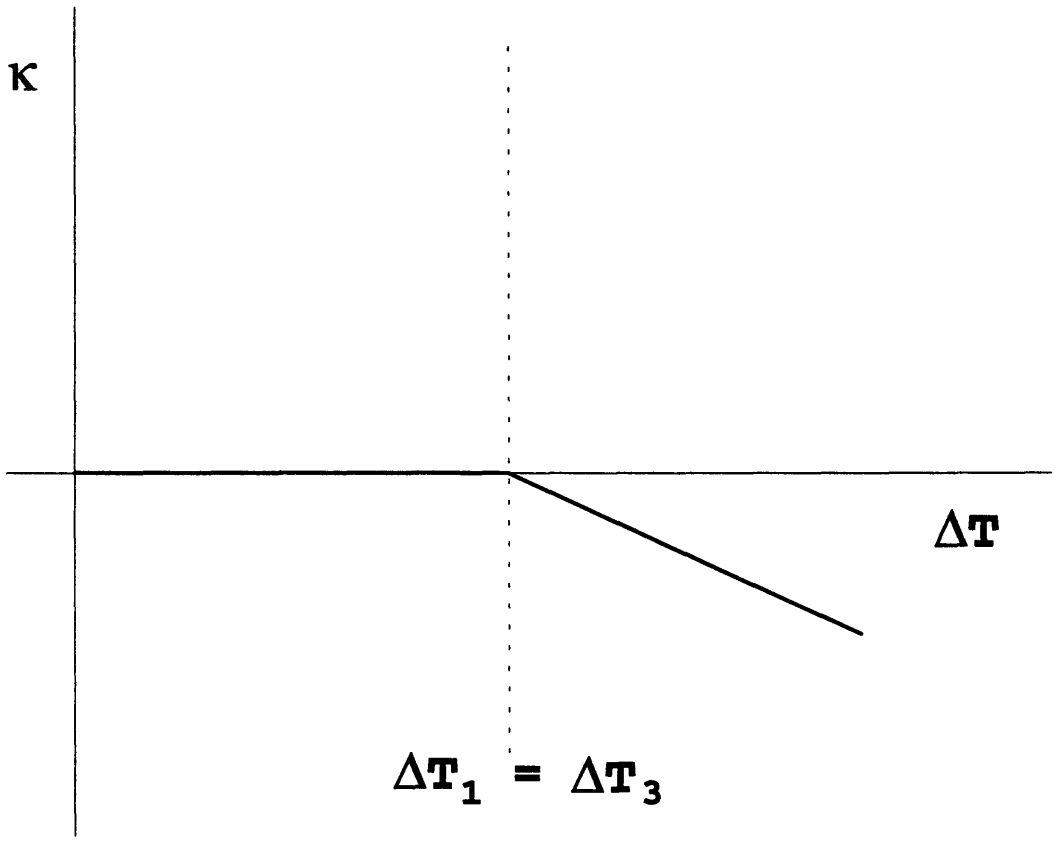

Figure B-15: Another type of κ-T schematic diagram with curvature reversal (critical condition).

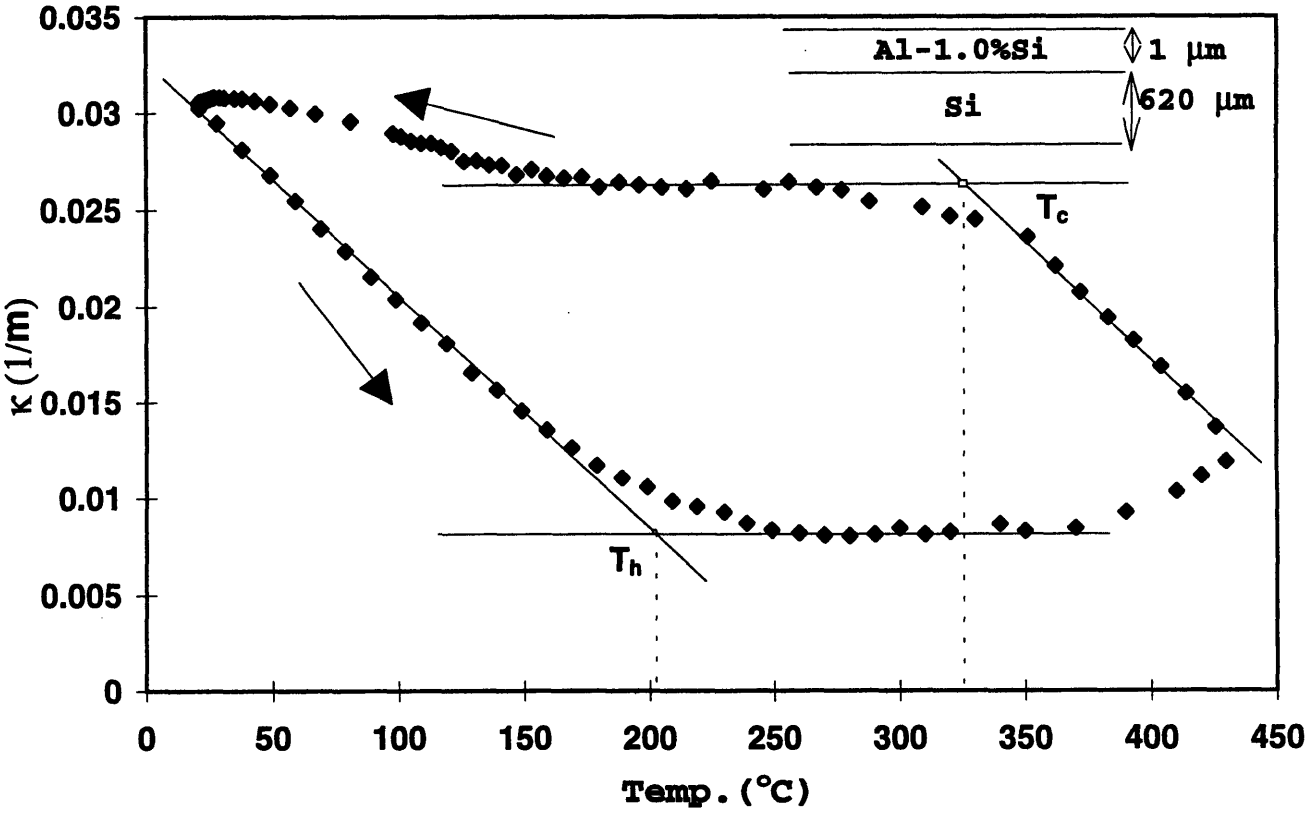

Figure B-16: The κ-T diagram for the bi-layer system Al(1% Si)-Si.

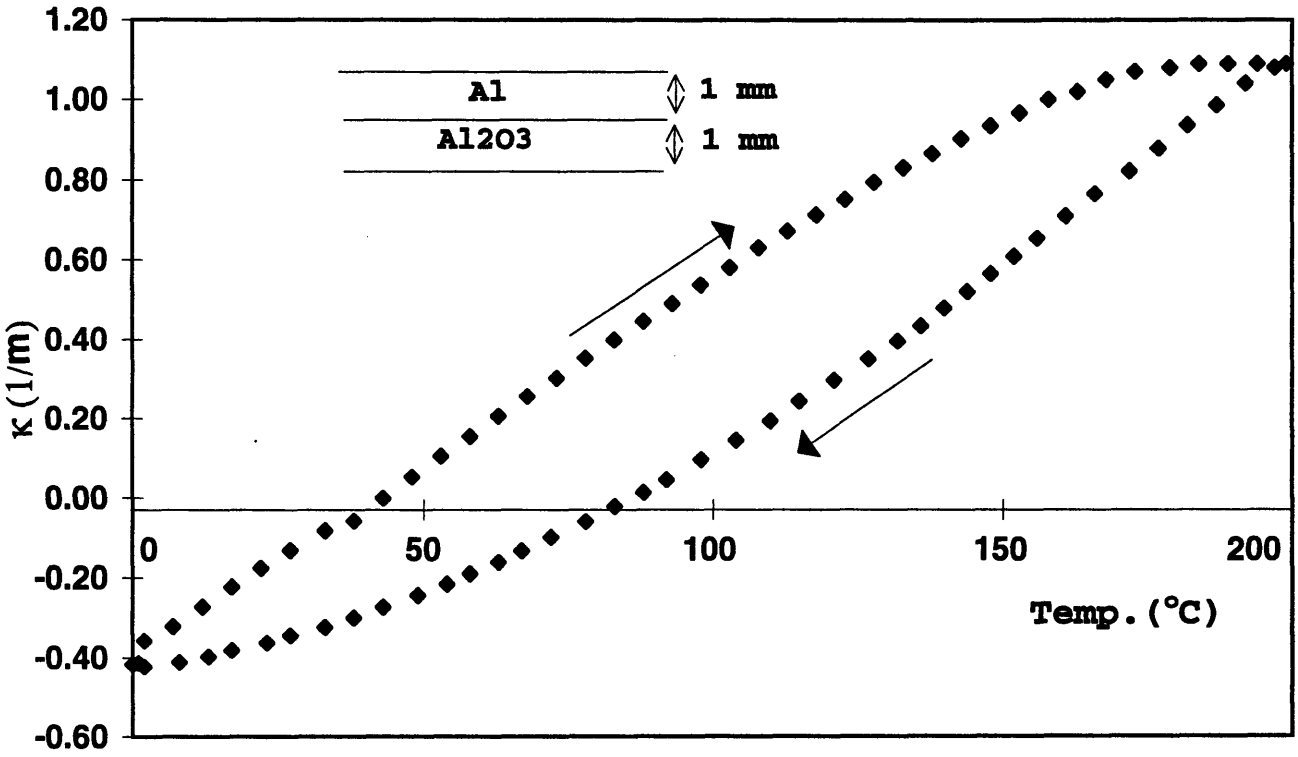

Figure B-17: The κ-T diagram for the bi-layer system Al-Al_2O_3.

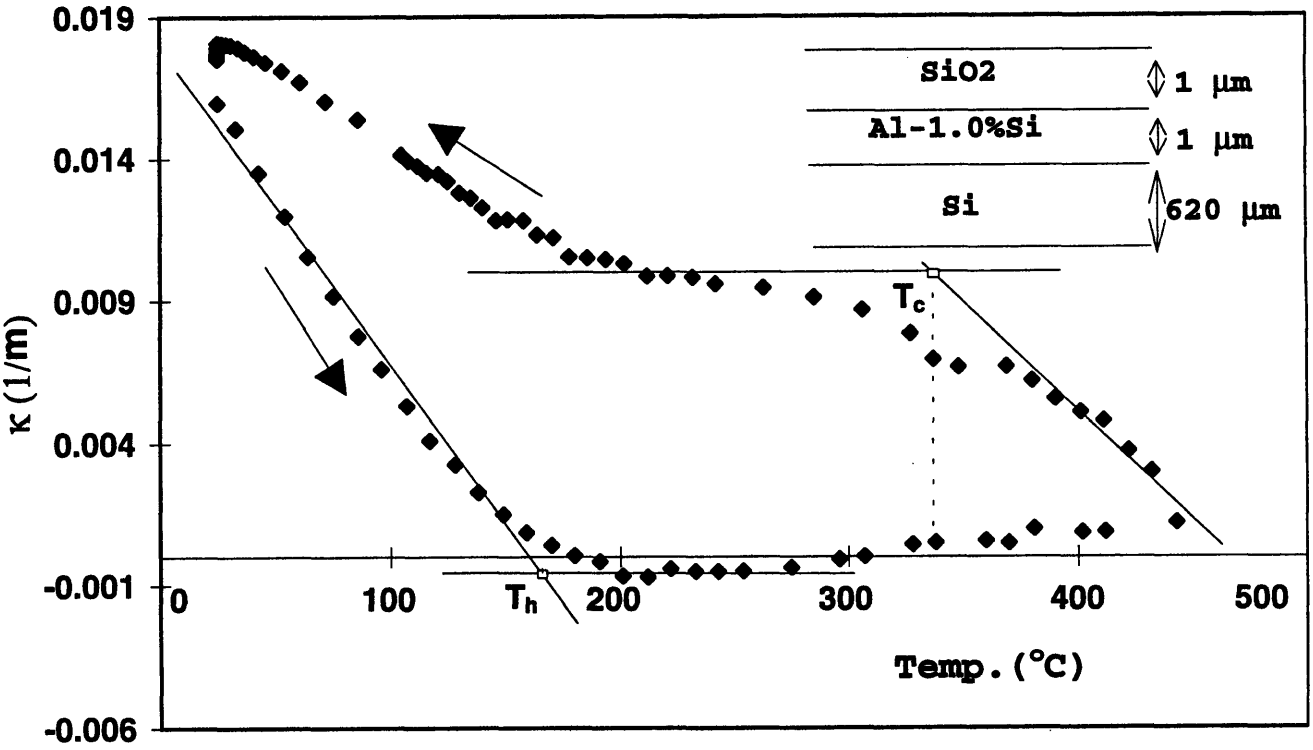

Figure B-18: The κ-T diagram for the tri-layer system Si-Al(1% Si)-SiO_2.

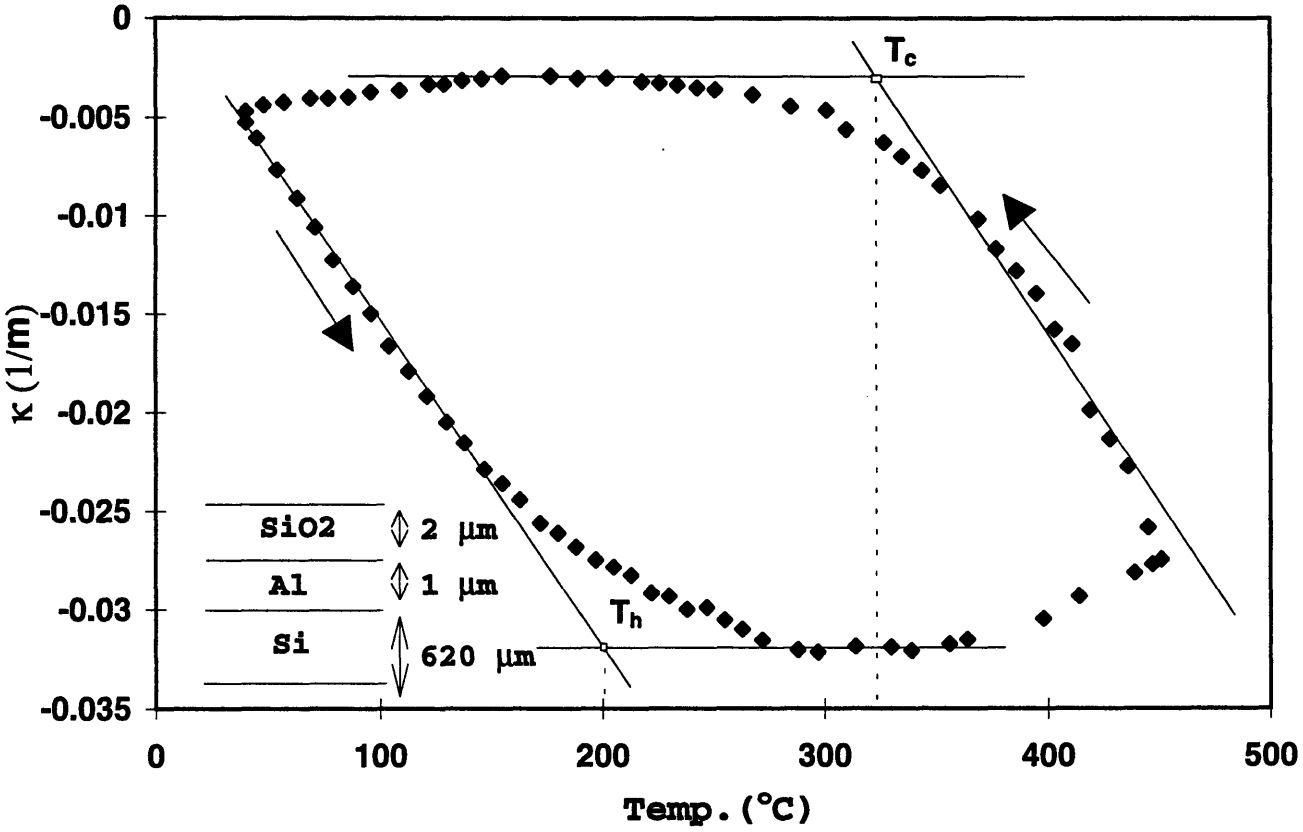

Figure B-19: The κ-T diagram for the tri-layer system Si-Al-SiO_2.

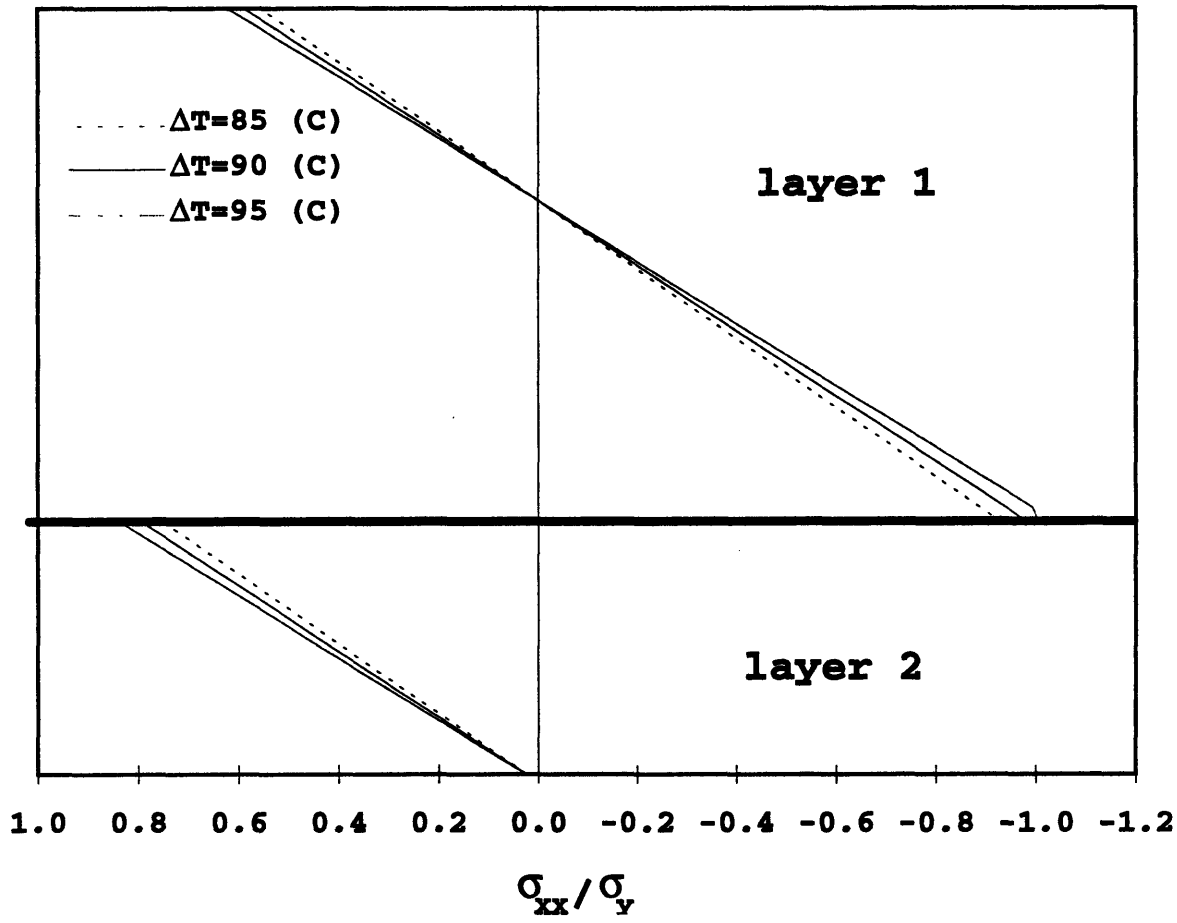

Figure B-20: The numerical results of the profiles of stress distribution in a bi-layer system with $\bar{E}_1/\bar{E}_2 = 1$ and $h_1/h_2 = 2$ at temperatures around ΔT_1.

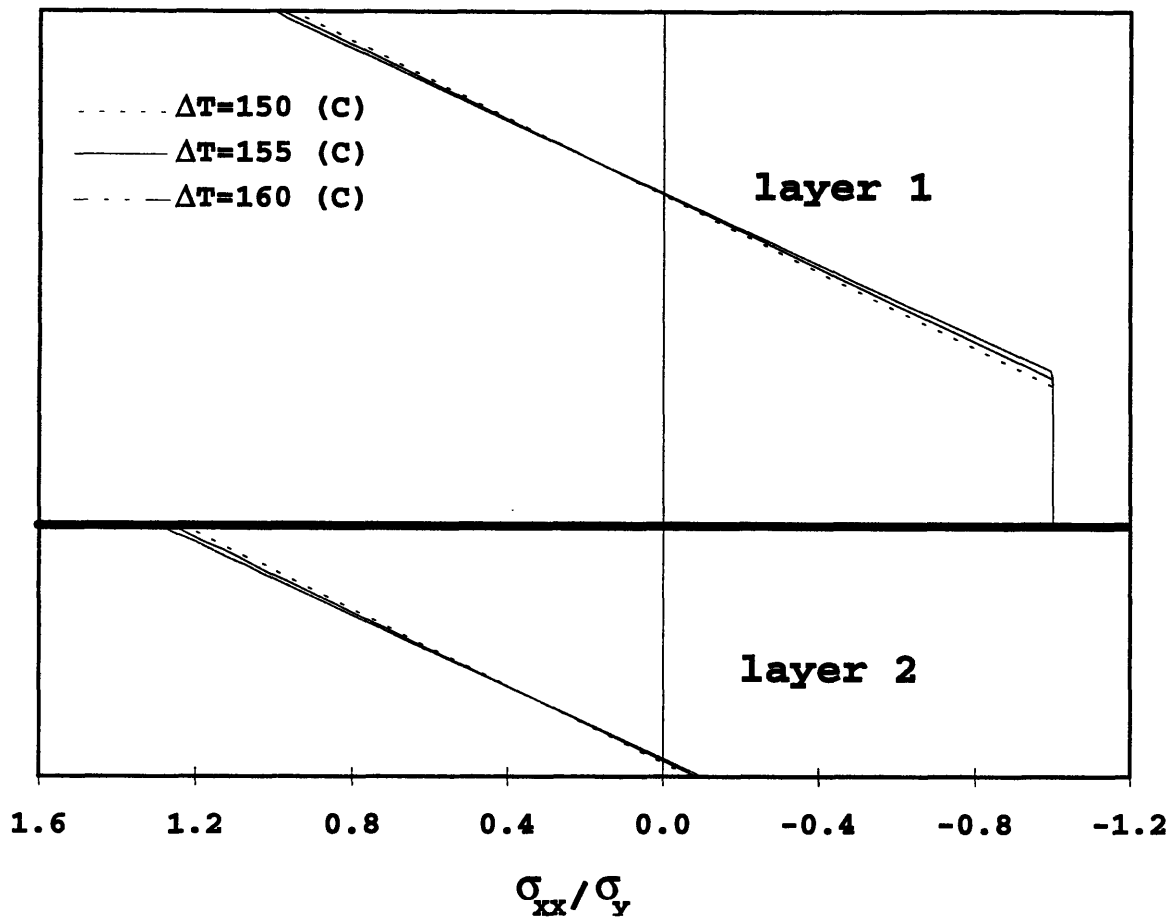

Figure B-21: The numerical results of the profiles of stress distribution in a bi-layer system with $\bar{E}_1/\bar{E}_2 = 1$ and $h_1/h_2 = 2$ at temperatures around ΔT_5.

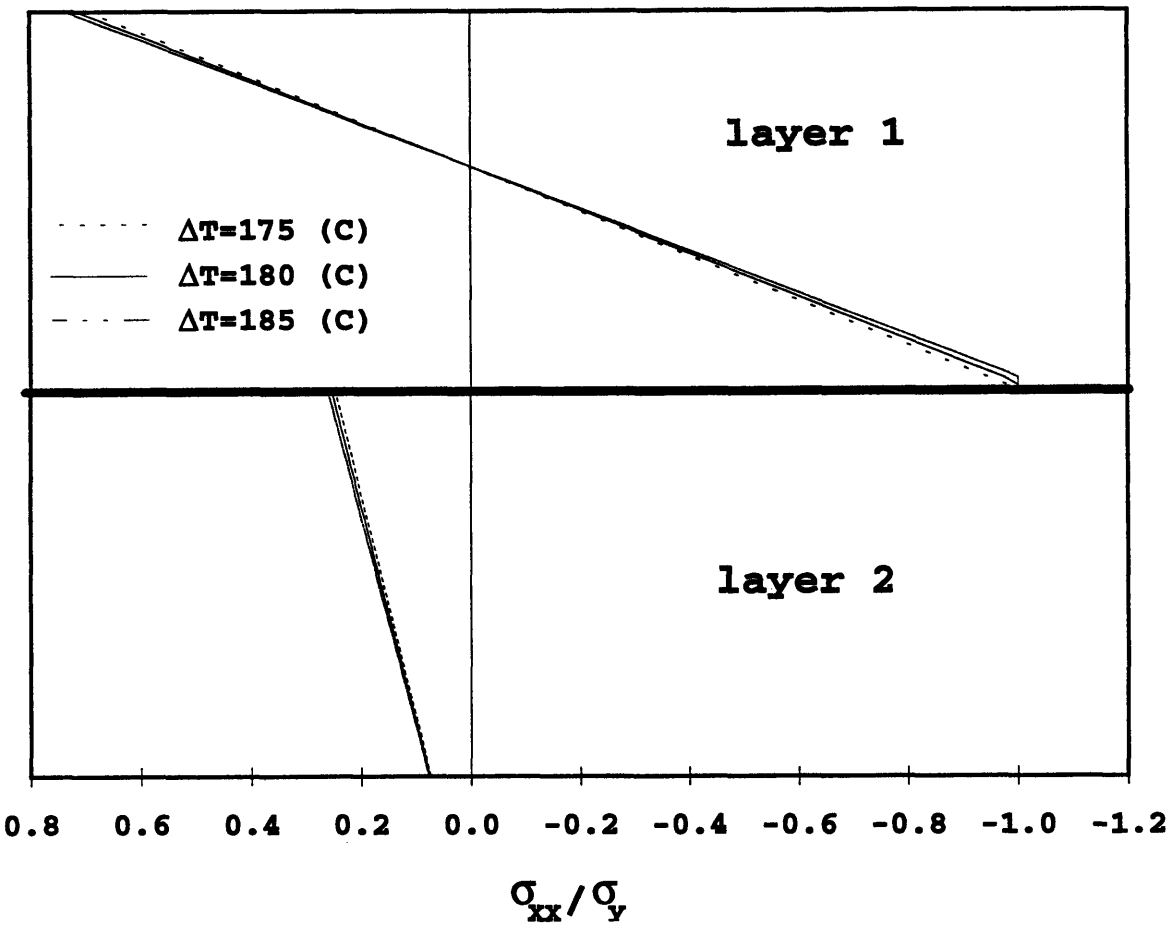

Figure B-22: The numerical results of the profiles of stress distribution in a bi-layer system with $\bar{E}_1/\bar{E}_2 = 10$ and $h_1/h_2 = 1$ at temperatures around ΔT_1.

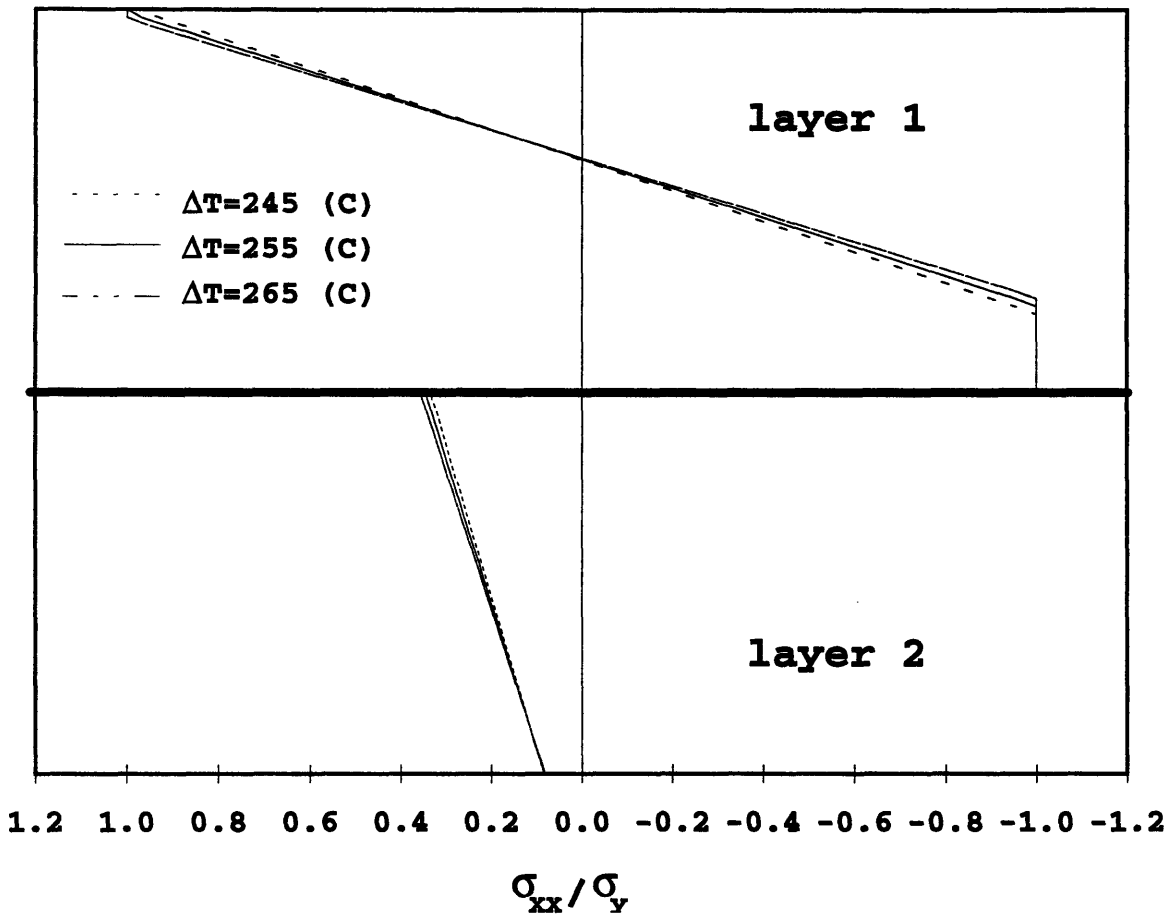

Figure B-23: The numerical results of the profiles of stress distribution in a bi-layer system with $\bar{E}_1/\bar{E}_2 = 10$ and $h_1/h_2 = 1$ at temperatures around ΔT_5.

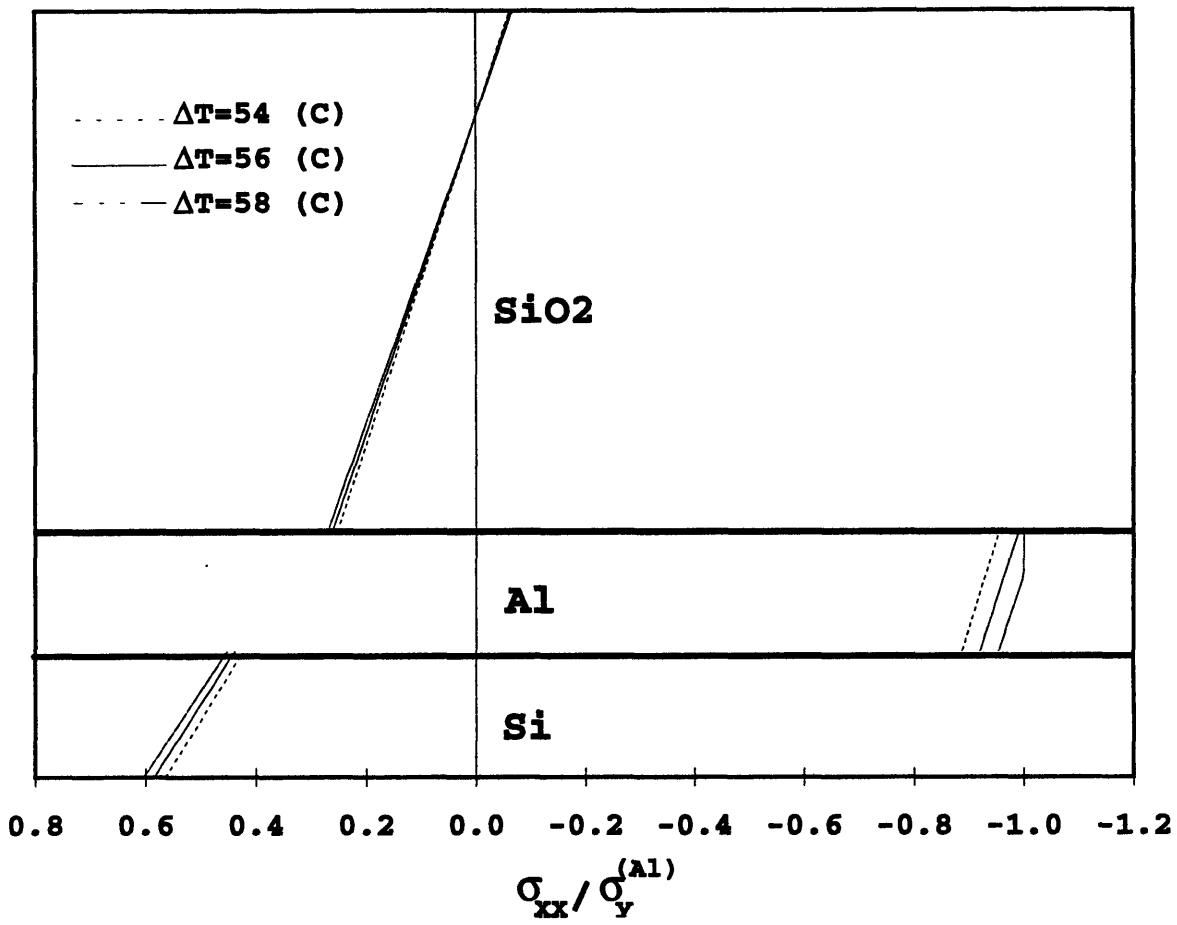

Figure B-24: The numerical results of the profiles of stress distribution in Si-Al-SiO_2 system with $h_2/h_1 = 1$ and $h_3/h_1 = 4$ at temperatures around ΔT_1.

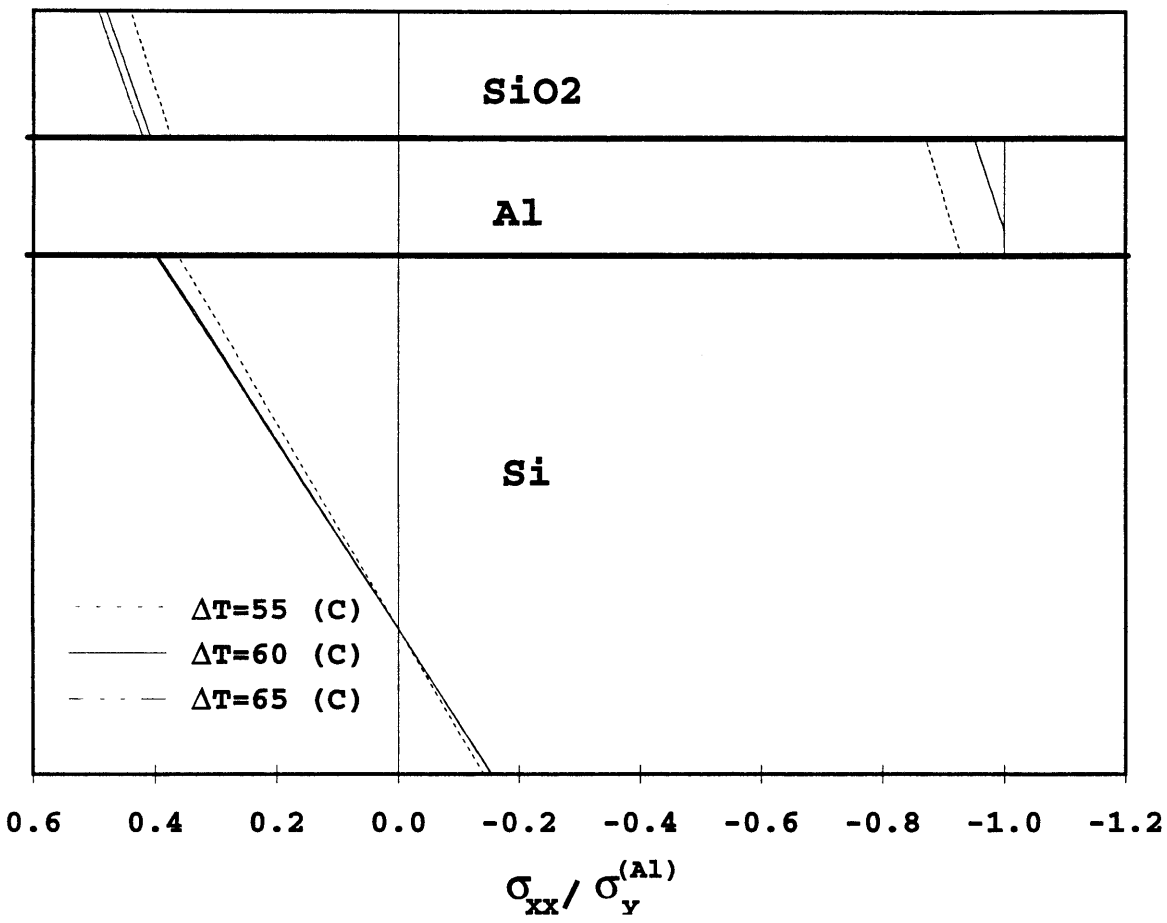

Figure B-25: The numerical results of the profiles of stress distribution in Si-Al-SiO_2 system with $h_2/h_1 = 4$ and $h_3/h_1 = 1$ at temperatures around ΔT_1.

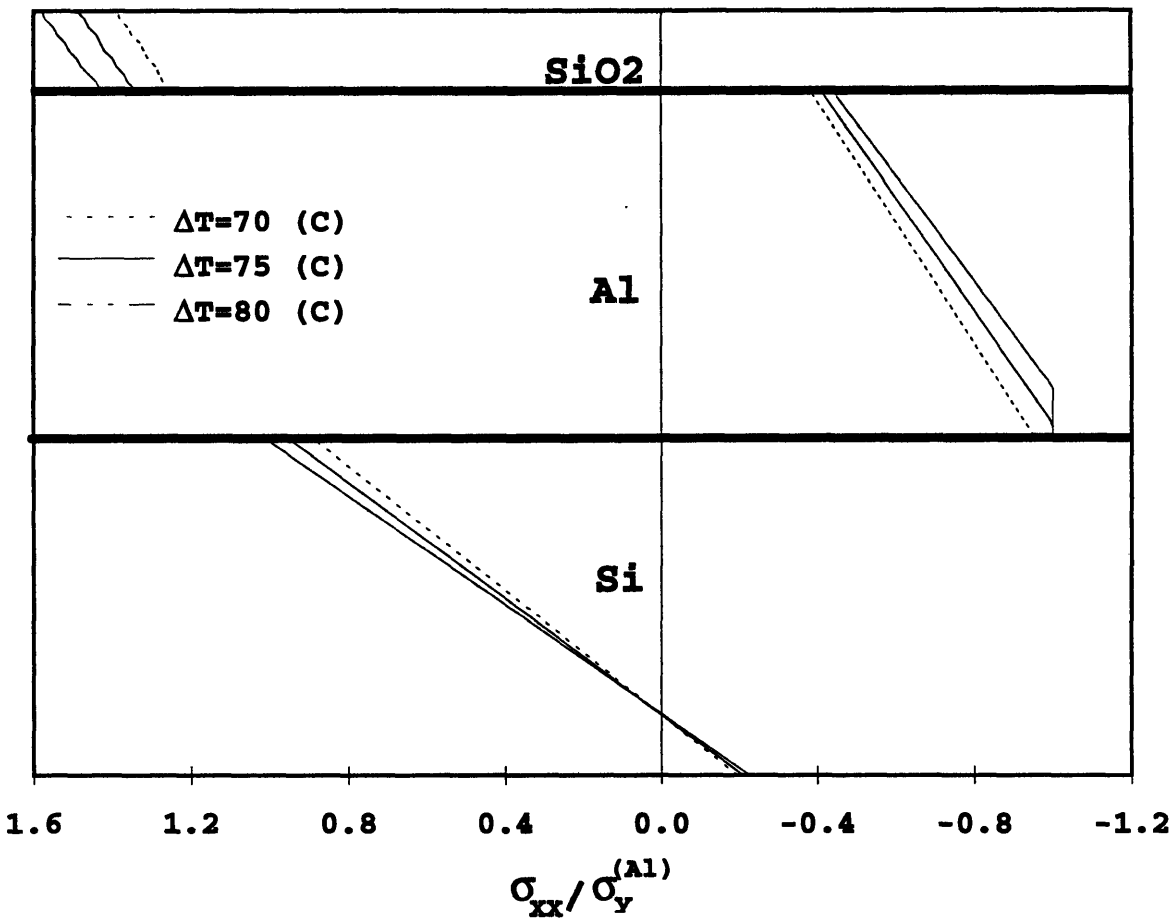

Figure B-26: The numerical results of the profiles of stress distribution in Si-Al-SiO_2 system with $h_2/h_1 = 1$ and $h_3/h_1 = 0.25$ at temperatures around ΔT_1.

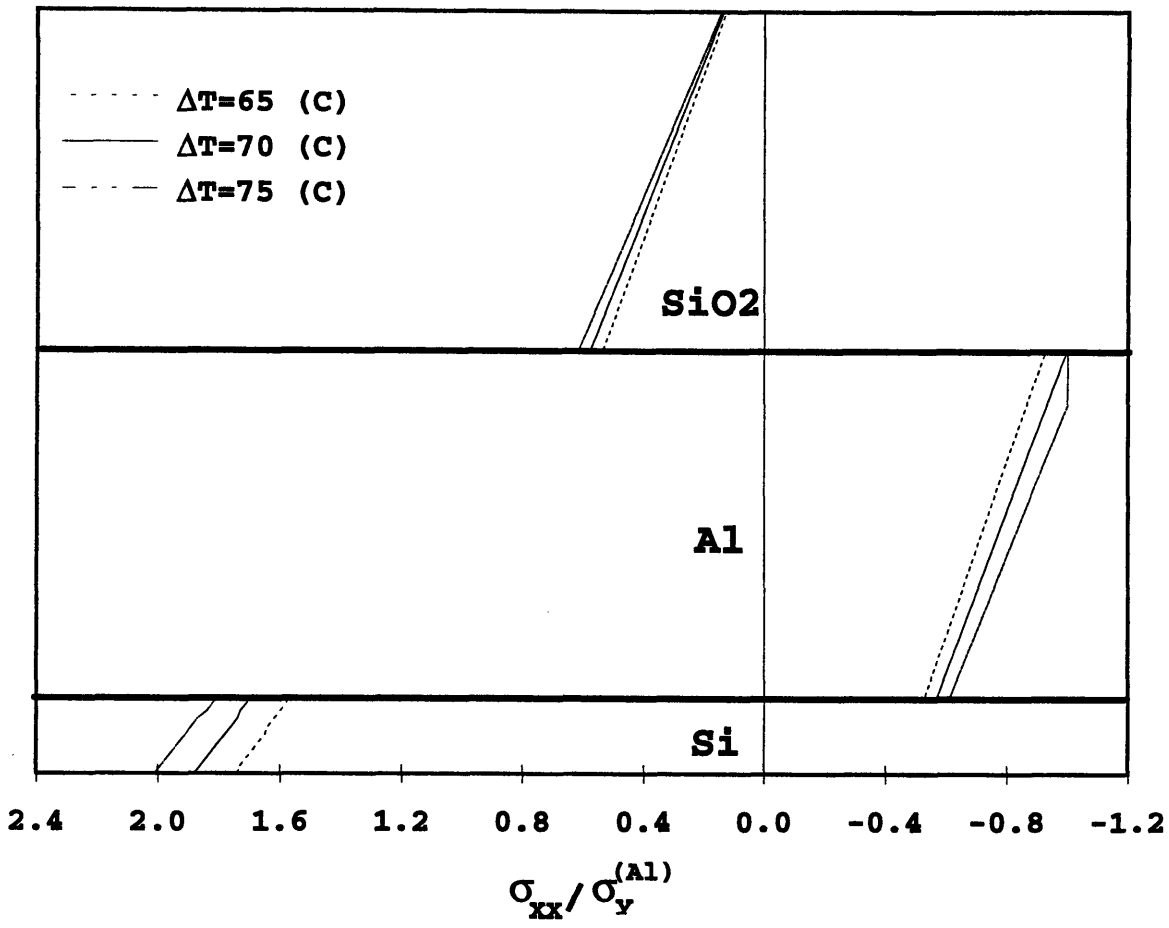

Figure B-27: The numerical results of the profiles of stress distribution in Si-Al-SiO_2 system with $h_2/h_1 = 0.25$ and $h_3/h_1 = 1$ at temperatures around ΔT_1.

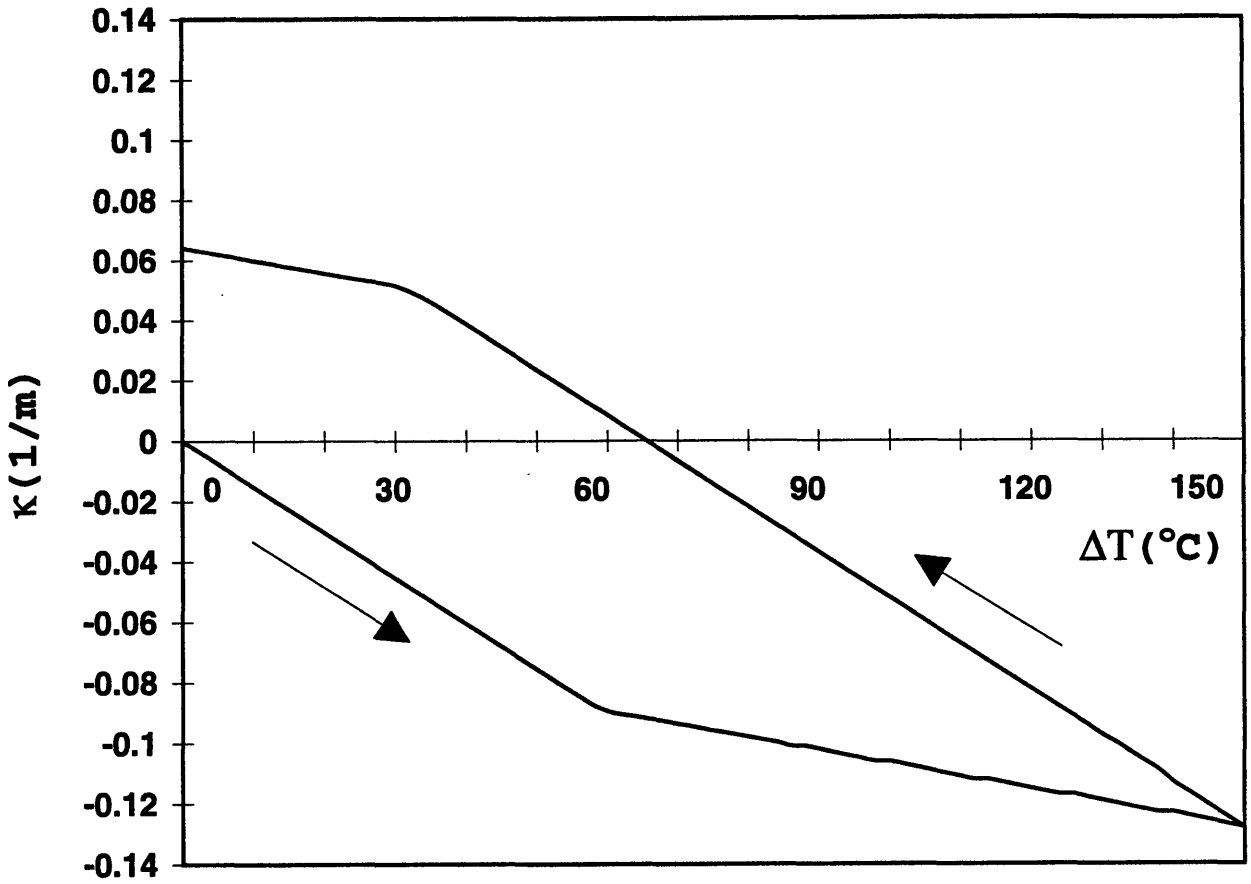

Figure B-28: The numerical results of the evolution of curvature in Si-Al-SiO_2 system with $h_2/h_1 = 1$ and $h_3/h_1 = 4$ during a cycle $\Delta T = 0°C \rightarrow 150°C \rightarrow 0°C$.

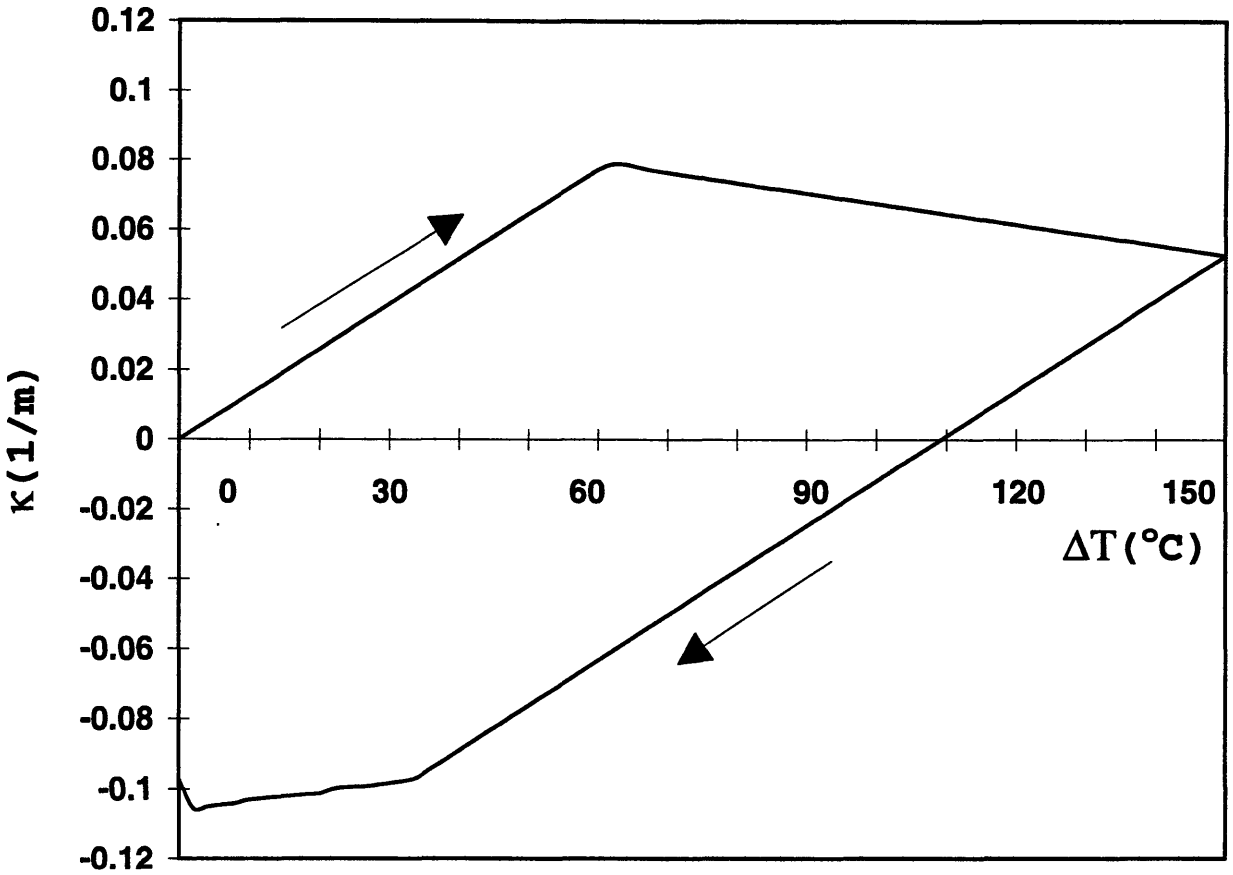

Figure B-29: The numerical results of the evolution of curvature in Si-Al-SiO_2 system with $h_2/h_1 = 4$ and $h_3/h_1 = 1$ during a cycle $\Delta T = 0°C \rightarrow 150°C \rightarrow 0°C$.

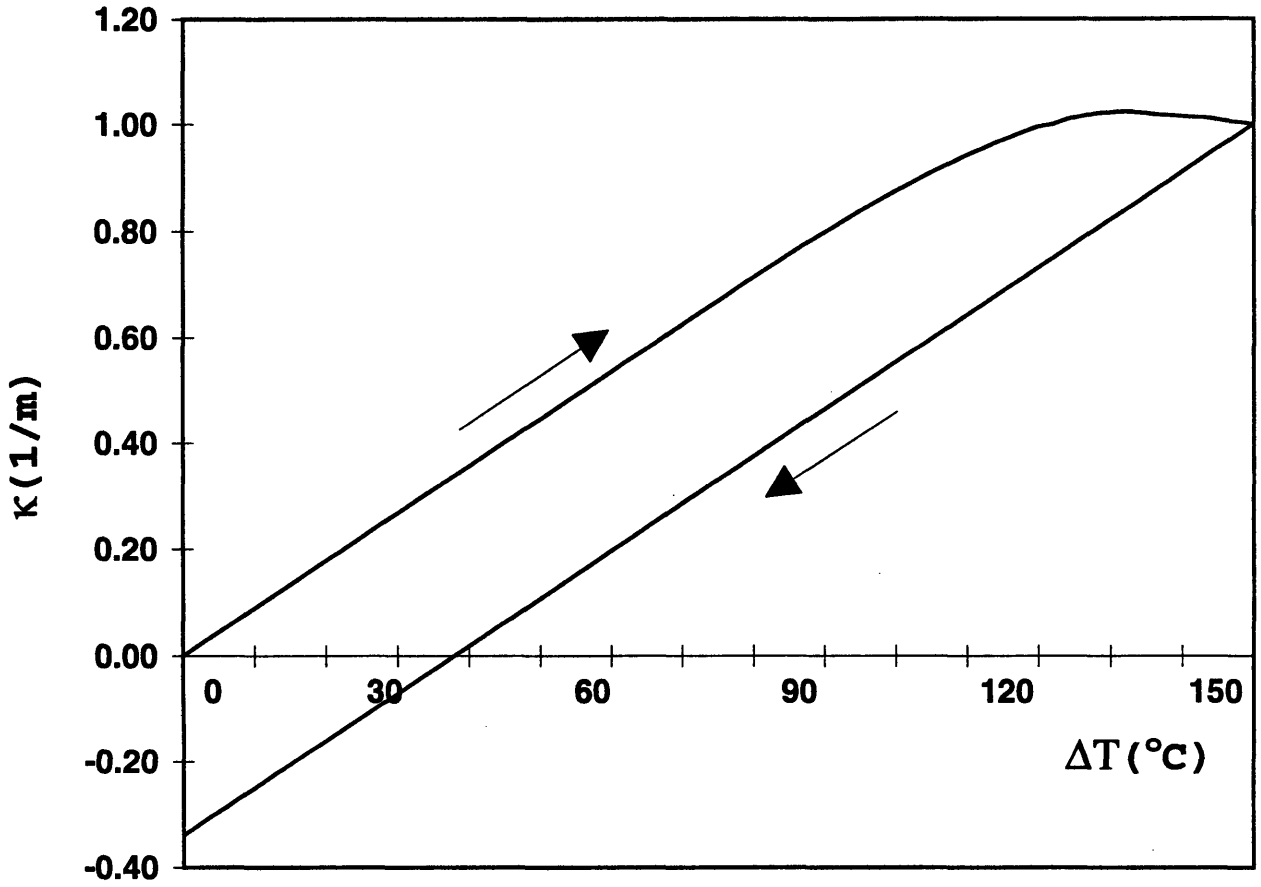

Figure B-30: The numerical results of the evolution of curvature in Si-Al-SiO_2 system with $h_2/h_1 = 1$ and $h_3/h_1 = 0.25$ during a cycle $\Delta T = 0°C \rightarrow 150°C \rightarrow 0°C$.

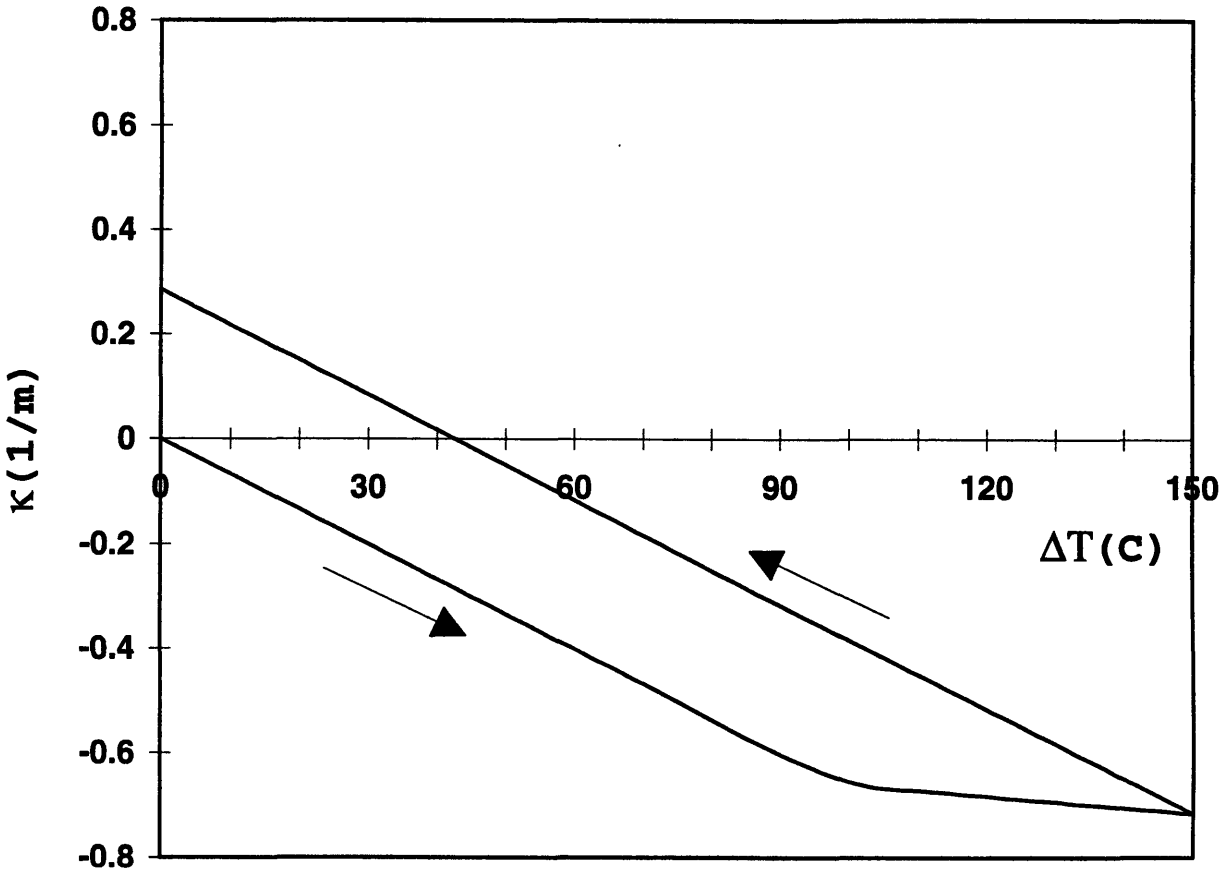

Figure B-31: The numerical results of the evolution of curvature in Si-Al-SiO_2 system with $h_2/h_1 = 0.25$ and $h_3/h_1 = 1$ during a cycle $\Delta T = 0°C \rightarrow 150°C \rightarrow 0°C$.

Bibliography

[1] G. G. Stoney. *Proc. R. Soc. Lond. A.*, 82:172+, 1909.

[2] A. Brenner and S. Senderoff. *J. Res. of National Bureau of Standards*, 42:105+, Feb. 1949.

[3] I. C. Noyan and L. T. Nguyen. *J. Polym. Sci. Engng.*, 28:1026+, 1988.

[4] B. D. Harper and G. P. Wu. *Int. J. Solids Structures*, 26:511+, 1990.

[5] M. F. Doerner, W. C. Oliver, G. M. Pharr, and F. R. Brotzen, editors. *Thin Films: Stresses and Mechanical Properties II*, Pittsburgh, PA, 1990.

[6] D. E. Fahnline, C. B. Masters, and N. J. Salamon. *J. Vac. Sci. Tech.*, pages 2483+, 1991.

[7] W. D. Nix, J. C. Bravman, E. Artz, and L. B. Freund, editors. *Thin Films: Stresses and Mechanical Properties III*, Pittsburgh, PA, 1992.

[8] J. Vilms and D. Kerps. *J. Appl. Phys.*, 53:1536+, 1982.

[9] Z. Feng and H. Liu. *J. Appl. Phys*, 54:83+, May 1983.

[10] E. Suhir. *J. Appl. Mech.*, 55:143+, 1988.

[11] P. H. Townsend, D. M. Barnett, and T. A. Brunner. *J. Appl. Phys.*, 62:4438+, 1987.

[12] L. B. Freund. *J. Crystal Growth*, 132:341+, 1993.

[13] S. Suresh, A. E. Giannakopoulos, and M. Olsson. *J. Mech. Phys. Solids*, 42:979+, 1994.

[14] Y. L. Shen and S. Suresh. *J. Mater. Res.*, 10:1200+, 1995.

[15] A. E. Giannakopoulos, S. Suresh, M. Finot, and M. Olsson. *Acta Metall. Mater.*, 43:1335+, 1995.

[16] M. Finot and S. Suresh. *J. Mech. Phys. Solids, in press.*

[17] S Timoshenko and J. N. Goodier. *Theory of Elasticity*, volume 2 of *The Art of Computer Programming.* McGraw-Hill, New York, 1951.

[18] P. A. Flinn, D. S. Gardner, and W. D. Nix. *IEEE Trans. Electron Dev.*, 34:689+, 1987.

[19] W. D. Nix. *Metall. Trans. A*, 20:2217+, 1989.

[20] M. Finot and S. Suresh. *MultiTherm: software for thermomechanical analysis of multi-layered and graded materials.* MIT copyright, Cambridge, MA, 1.3 edition, 1994.

[21] M. Finot, S. Suresh, C. Bull, and S. Sampath. *Mater. Sci. Eng. in press.*

[22] Ramnath Venkatraman, J. C. Bravman, and W. D. Nix. *J. of Elec. Matls.*, 19:1231+, 1990.

[23] Y. L. Shen and S. Suresh. *Acta Metall. Mater. in press.*

[24] M. G. Hocking, V. Vasantasree, and P. S. Sidky. *Metallic and Ceramic Coatings.* Longman Scientific Technical, England, 1989.

[25] *ASM Handbook*, volume 5. ASM International, Materials Park, OH, 10th edition, 1990.

[26] K. Holmberg and A. Matthews. *Tribology series 28: Coatings Tribology.* Elsevier Science, The Netherlands, 1994.

[27] B. Bhushan and B. K. Gupta. *Handbook of Trobology.* McGraw-Hill, New York, 1991.

[28] H. L. Tsai and P. C. Tsai. *Mater. Sci. Eng. A*, 177:227+, 1994.

[29] J. H. Sun, E. Chang, C. H. Chao, and M. J. Cheng. *Oxidation of Metals*, 40:465+, 1993.

[30] I. Smurov, A. Uglov, Y. Krivonogov, S. Sturlese, and C. Bartuli. *J. Mater. Sci.*, 27:4523+, 1992.

[31] D. J. Wortman, B. A. Nagaraj, and E. C. Duderstadi. *Mater. Sci. Eng. A*, 120:433+, 1989.

[32] S. Stecura. *Thin Solid Films*, 136:241+, 1986.

[33] C. C. Berndt. *J. Eng. Gas Turbines Power-Trans. ASME*, 107:142+, 1985.

[34] J. C. Colson and J. P. Larpin. *Mater. Sci. Eng.*, 87:11+, 1987.

[35] M. Van De Voorde. *Mater. Sci. Eng.*, 88:341+, 1987.

[36] A. F. Taylor. In K. N. Strafford, P. K. Datta, and C. G. Goodgan, editors, *Coatings and Surface Treatment for Corrosion and Wear Resistance*, pages 213+. Ellis Horwood Limited, England, 1984.

[37] T. Fransen, E. Polman, and M. M. A. Perik. In W. Betz, R. Brunetaud, D. Coutsouradis, H. Fischemeister, T. B. Gibbons, I. Kvernes, Y. Lindblom, J. B. Marriott, and D. B. Meadowcroft, editors, *High Temperature alloys for Gas Turbines and Other Applications PART II*, pages 1157+. D. Reidel Publishing, Holland, 1986.

[38] Y. L. Shen. *research in progress*, 1995.

[39] E. M. Coudert and Y. Murakami. *Mater. Sci. Res. Intl.*, 1:37+, Mar. 1995.

[40] R. Doherty, K. Kashyap, and S. Panchanadeeswaran. *Acta Metall. Mater.*, 41:3029+, 1993.

[41] W. A. Glasesea. *Tribology series 20: Materials for Tribology.* Elsevier Science, The Netherlands, 1992.

[42] J. F. Lynch, C. G. Ruderer, and W. H. Duckworth, editors. *Engineering Properties of Selected Ceramic Materials.* American Ceramic Society, Ohio, 1966.

[43] J. R. Hague, J. F. Lynch, A. Rudnick, F. C. Holden, and W. H. Duckworth. *Refractory Ceramics of Interest in Aerospace Structural Applications - A Materials Selection Handbook.* Technical documentary Report No. ASD-TDR-63-4102, Wright-Patterson Air Force Base, Ohio, Oct. 1963.

[44] C. A. Hampel. *Rare Metals Handbook.* Reinhold Pub. Corp., New York, second edition, 1961.

[45] A. Prince, editor. *Handbook of Precious Metals.* Hemisphere Pub. Corp., New York, 1989.

[46] M. A. Filyand, E. I. Semenova, (translated, and edited by M. E. Alferieff). *Handbook of the Rare Elements.* Boston Technical, Cambridge, MA, 1968.

[47] *ASM Handbook*, volume 1. ASM International, Materials Park, OH, 10th edition, 1990.

[48] *ASM Handbook*, volume 2. ASM International, Materials Park, OH, 10th edition, 1990.